UA-ICON with NWP physics package (version: ua-icon-2.1): mean state and variability of the middle atmosphere

Markus Kunze[1], Christoph Zülicke[1], Tarique A. Siddiqui[1,*], Claudia C. Stephan[1], Yosuke Yamazaki[1], Claudia Stolle[1], Sebastian Borchert[2], and Hauke Schmidt[3]

[1]Leibniz Institute of Atmospheric Physics at the University of Rostock, Kühlungsborn, Germany
[2]Deutscher Wetterdienst, Offenbach am Main, Germany
[3]Max Planck Institute for Meteorology, Hamburg, Germany
[*]now at Centre for Artificial Intelligence in Public Health Research (ZKI-PH), Robert Koch Institute, Berlin, Germany

Correspondence: Markus Kunze (kunze@iap-kborn.de)

Abstract. The Icosahedral Nonhydrostatic (ICON) general circulation model with upper atmosphere extension (UA-ICON) in the configuration with the physics package for numerical weather prediction (NWP) is presented with optimized parameter settings for the non-orographic and orographic gravity wave drag parameterizations (GWD), UA-ICON(NWP) (version: ua-icon-2.1). We implemented optimized parameter settings for the GWD parameterizations to achieve more realistic MLT temperatures and zonal winds. The parameter optimization is based on perpetual January simulations targeting the thermal and dynamic state of the MLT and the Northern Hemisphere stratosphere. The climatology and variability of the Northern Hemisphere stratospheric winter circulation widely improve when applying UA-ICON with the NWP physics package compared to UA-ICON with ECHAM physics. Likewise improves the thermal and dynamic state of the MLT of the re-tuned UA-ICON(NWP) compared with the UA-ICON(NWP) using default settings. A statistical evaluation of UA-ICON(NWP) reveals a slight improvement in the stratosphere/mesosphere coupling compared to UA-ICON(ECHAM). The cold summer mesopause, the warm winter stratopause, and the related wind reversals are reasonably simulated. The GWD parameter optimization further significantly improves the frequency of major sudden stratospheric warmings (SSWs). However, the seasonal distribution needs improvement and the relative frequency of split vortex SSWs is underestimated compared to reanalyses, as is the zonal wavenumber 2 preconditioning of SSWs. This indicates that zonal wavenumber 2 forcing in UA-ICON(NWP) is underrepresented. The analysis of migrating diurnal and semidiurnal tides in temperature shows a good agreement of UA-ICON(NWP) with SABER-derived tides and the enhancement of the migrating semidiurnal tide during SSWs is well represented in UA-ICON(NWP).

1 Introduction

The mesopause region is the transition region between the middle and upper atmosphere. Its circulation is mainly driven by breaking gravity waves and the associated momentum flux divergence, driving the meridional residual circulation resulting in temperatures far away from radiative equilibrium in the mesosphere/lower thermosphere (MLT). This is reflected in the low atmospheric temperatures in the summer mesopause region with monthly mean minima below 140 K. These very low

temperatures enable phenomena such as the noctilucent clouds (NLCs) in high latitudes at an altitude between 82 and 85 km (e.g., Berger and von Zahn, 2002). General circulation models (GCMs) which include the MLT are, e.g., WACCM (Richter

25   et al., 2008, 2010; Gettelman et al., 2019), WACCM-X (Liu et al., 2018a), GAIA (Jin et al., 2012), the extended CMAM (eCMAM) (Beagley et al., 2000; Fomichev et al., 2002), HAMMONIA (Schmidt et al., 2006), HIAMCM (Becker and Vadas, 2020), KMCM (Becker, 2009), JAGUAR (Watanabe and Miyahara, 2009) and UA-ICON (Borchert et al., 2019), the upper atmosphere extension of the Icosahedral Nonhydrostatic (ICON) general circulation model (Zängl et al., 2015).

Concerning physics, ICON is equipped with two different packages. One is based on physics from the ECHAM model and

30   is now further developed at the Max Planck Institute for Meteorology (MPI-M). The other package, NWP, is maintained by the German Meteorological Service (Deutscher Wetterdienst, DWD). For applications with low horizontal resolutions relying on gravity wave parameterization, as presented here, the NWP package is the only choice in the current development of the ICON model. The initial UA-ICON version, as presented by Borchert et al. (2019), included both physics packages, however, the majority of the results are based on the ECHAM physics package which is no longer part of the actual development. Instead,

35   we use the NWP package here to validate its performance in the mesopause region, which has not been done so far.

An outstanding feature of ICON, and by this of UA-ICON, is its capability to apply several nests of successively higher horizontal resolutions embedded in a global coarser grid. Among the GCMs with extensions into the thermosphere, applying flexible subsequent grid refinements is a unique feature of UA-ICON. In the recent WACCM development with regional grid refinement (WACCM-RR), one finer grid is embedded in the global grid. Related studies at different model resolutions using

40   UA-ICON are available with the application of both physics packages. For UA-ICON(ECHAM) these include Stephan et al. (2020), analysing oblique gravity wave (GW) propagation during one minor SSW in ∼20 km (referred to as R2B7 grid) simulations without GW-drag (GWD) parameterization. Applications of UA-ICON(ECHAM) in its original horizontal mesh size of ∼160 km (R2B4), as evaluated by Borchert et al. (2019), are given in Stober et al. (2021) and Wallis et al. (2023). Stober et al. (2021) used several GCMs with upper atmosphere extensions (amongst these UA-ICON(ECHAM)) to evaluate

45   the performance of the models concerning winds and tides in the MLT, in comparison to winds derived from meteor radar at northern and southern latitudes, and to analyse inter-hemispheric coupling. In this comparison, the free-running UA-ICON performed relatively well in modelling the MLT wind fields compared to the otherwise nudged models. Recently, Wallis et al. (2023) used UA-ICON(ECHAM) to analyse the effect of an idealized large tropical volcanic eruption in June on the temperature structure in the mesosphere. Applications using the UA-ICON(NWP) configuration at a coarse horizontal resolution of ∼160

50   km (R2B4) are provided in Karami et al. (2022, 2023); Kim and Achatz (2021); Kim et al. (2021); Bölöni et al. (2021). They have either used the standard non-orographic gravity wave drag (NGWD) parameterization (Orr et al., 2010; Warner and McIntyre, 1996), namely Karami et al. (2022, 2023), or introduced a new NGWD parameterization overcoming the steady-state assumptions currently used in standard NGWD parameterizations (Bölöni et al., 2021; Kim et al., 2021; Kim and Achatz, 2021). In our tuning experiments, we also consider the effects of orographic gravity waves (OGW) which directly influence

55   the stratospheric vortex and by this, indirectly, the mesospheric circulation. Higher horizontal resolutions of UA-ICON(NWP) with a global ∼20 km grid spacing (R2B7), and the application of two additional nests with higher horizontal resolutions of

∼10 km (R2B8) and ∼5 km (R2B9), respectively, were used in the study of Charuvil Asokan et al. (2022) for the validation of vertical and horizontal winds derived from meteor radar observations.

The main objective of this work is to document the tuning requirements of the GWD parameterization for UA-ICON(NWP), which is necessary for its application with the coarse horizontal resolution of R2B4. Simulations with a coarse resolution are a prerequisite for short-term experiments with higher-resolution nests and long-term climatological studies. We use several climatologies, mainly based on satellites, as references for these global simulations. This is done for the primary meteorological quantities like wind and temperature. More dedicated quantities like wave drag are compared with other models. Besides the seasonal cycle of the middle atmosphere, we also investigate major sudden stratospheric warmings during the NH winter season (in the following abbreviated with SSWs), which are the most dramatic changes in the stratosphere with large temperature changes in the polar region within a couple of days (Scherhag, 1952). A large increase in temperature in polar regions also affects the zonal wind which is decelerated, and in the case of major SSWs can turn from the usual zonal mean eastward-directed flow to a zonal mean westward-directed flow. SSWs are forced by the dissipation of upward propagating large-scale planetary (Rossby) waves (Charney and Drazin, 1961). The reviews of Baldwin et al. (2021) and Butchart (2022) summarize the research and progress in understanding the causes and consequences of SSWs over the past 70 years. A satellite-based benchmark test, including the mesosphere, was developed by Zülicke et al. (2018) and will be used in the present study to analyse SSW effects.

Finally, we identify atmospheric tides in UA-ICON and their behaviour concerning SSWs. Atmospheric tides are global-scale oscillations with a period of a day and its harmonics (Chapman and Lindzen, 1969). Solar tides are thermally driven by periodic heating due to the absorption of solar radiation mainly by water vapor in the troposphere and ozone in the stratosphere (Forbes and Garrett, 1979), as well as due to latent heat release in the deep tropical convection (Zhang et al., 2010a, b). Tides generated in the troposphere and stratosphere grow in amplitude as they propagate vertically into the MLT region where they achieve their maximum amplitudes (Hagan and Forbes, 2002, 2003; Oberheide et al., 2011). MLT tides are important in driving the upper atmosphere including the ionosphere (Yamazaki and Richmond, 2013; Jones et al., 2014). Global observations from satellites have established that westward-propagating solar 'migrating' (i.e., Sun-synchronous) diurnal (24 h) and semidiurnal (12 h) tides are the dominant modes of MLT tides (McLandress et al., 1996; Forbes et al., 2008; Yamazaki et al., 2023). Thus, we will focus on these tidal modes.

We introduce the UA-ICON model and the data used for evaluation in Sect. 2. In Sect. 3 we evaluate the seasonal averages of the zonal wind and temperature around the solstices for UA-ICON(NWP) after optimizing the GWD parameterizations. Section 4 summarizes the tuning process for the GWD parameterizations performed in a perpetual January setup. An evaluation of the northern hemispheric winter variability and the statistics of major SSWs are presented in Sect. 5. Sect. 6 is devoted to the simulation of thermal tides compared to SABER observations. The final Sect. 7 concludes with a discussion and a summary.

2 Model, data and methods

2.1 Model and setup

90 ICON is a joint development of the DWD, the MPI-M, Deutsches Klimarechenzentrum (DKRZ), the Karlsruhe Institute of Technology (KIT), and the Center for Climate Systems Modeling (C2SM) to create a modelling framework that serves the need for numerical weather prediction (NWP) as well as the application for climate simulations. For these tasks originally two physics packages with sets of parameterizations have been available, namely NWP (Zängl et al., 2015) for weather prediction and ECHAM for climate applications (Giorgetta et al., 2018; Jungclaus et al., 2022). ICON employs a non-hydrostatic dynam-

95 ical core on an unstructured triangular C-grid, and a geometric altitude grid, which is terrain-following up to a certain height. A Lorenz-type staggering is applied in the vertical with the prognostic variables of the grid-edge-normal wind components,

Process	ua-icon-1.02 (ECHAM)	ua-icon-2.1 (NWP)
Longwave (LW) and Shortwave (SW) radiation	PSRAD (Pincus and Stevens, 2013), (based on RRTM, Mlawer et al., 1997)	ecRAD (Hogan and Bozzo, 2016), (based on RRTM, Mlawer et al., 1997)
Turbulent transfer	ECHAM6.3 Pithan et al. (2015)	Prognostic turbulence kinetic energy (TKE) (COSMO, default) Raschendorfer (2001)
Cloud cover	Diagnostic Sundqvist et al. (1989)	Diagnostic probability density function (PDF) M. Köhler et al. (DWD) (default)
Convection	Tiedtke (1989)/Nordeng (1994)	Tiedtke (1989)/Bechtold et al. (2008) (default)
Cloud microphysics	Single-moment scheme Lohmann and Roeckner (1996)	Single-moment scheme (default) Doms et al. (2011), Seifert (2008)
Non-orographic GWD	Hines (1997a, b)	Orr et al. (2010) (IFS), (based on Warner and McIntyre, 1996)
Subgrid scale orographic effects (SSO)	Lott and Miller (1997); Lott (1999)	Lott and Miller (1997) (COSMO, default)

Table 1. Parameterizations for physical processes given in the first column in UA-ICON simulations with ECHAM physics (second column) and NWP physics package (third column).

the potential temperature, and the density of moist air defined on full model levels and the vertical wind component defined on the half levels. The main parameterizations of the NWP and ECHAM physics packages, as applied in this work, are listed in Table 1. ICON's upper atmosphere (UA) extension consists of an optional deep-atmosphere dynamical core and supplementary

100 physical parameterizations for the relevant physical processes in the MLT (Borchert et al., 2019). These are parameterizations for molecular diffusion (Huang et al., 1998), ion-drag and Joule heating (Hong and Lindzen, 1976), frictional heating (Gill, 1982), the heating rates of O_2 absorption of ultraviolet (UV) in the Schumann-Runge bands and continuum (Strobel, 1978), absorption of extreme-UV by N_2, O, and O_2 (Richards et al., 1994), non-LTE infrared cooling by CO_2, NO, and O_3 (Fomichev and Blanchet, 1995; Fomichev et al., 1998; Ogibalov and Fomichev, 2003), and infrared NO cooling at 5.3μm (Kockarts,

1980). UA-ICON does not include interactive chemistry and describes the chemical heating with a climatological annual cycle from a 30-year time slice simulation of HAMMONIA (Schmidt et al., 2006).

The ICON release icon-2024.01-1 (ICON partnership (DWD, MPI-M, DKRZ, KIT, and C2SM), 2024) is the code basis in this work whenever using the NWP physics package (ua-icon-2.1). In contrast, the UA-ICON simulation using the ECHAM physics package is based on a slightly updated version of Borchert et al. (2019) (ua-icon-1.02). The model code used in this study is published on Zenodo (Kunze et al., 2024). It is based to a large extent on Fortran. We checked the code quality with FortranAnalyser (García-Rodríguez et al., 2024) and obtained a final score of 4.1, which is a relatively high score compared to the existing climate models (M. García-Rodríguez, personal communication, February 16, 2025). The ICON model code is largely equipped with OpenACC directives and in special configurations ICON has been deployed on GPU computing architectures (Giorgetta et al., 2022). However, the upper atmosphere extension is not ported to GPU and we performed our model simulations on the CPU architecture of the DKRZ (German Climate Computing Center) HPC system. Using the message-passing interface with 20 cores and 2560 processors, one year of simulation requires a wall-clock time of 62 minutes.

All simulations in this work use the R2B4 horizontal resolution, corresponding to a grid distance of $\sim$160 km, and 120 levels up to 150 km. They all apply the upper-atmosphere (UA) extension of ICON, described by Borchert et al. (2019) for the ECHAM and the NWP physics packages.

Simulation	Version (Git tag)	Physics	Years	Setup
UA-ICON(ECHAM)	ua-icon-1.02	ECHAM	20	Borchert et al. (2019)
UA-ICON(NWPD)	ua-icon-2.1	NWP	60	F1C1
UA-ICON(NWP)	ua-icon-2.1	NWP	60	F2C30-S

Table 2. UA-ICON time slice simulations with a seasonal cycle, with the columns indicating the simulation's label, the version, the physics package, the number of years after a one-year spin-up, and the setup. Table 3 details the simulation's setup with NWP physics.

Three time-slice simulations with a seasonal cycle are presented here with boundary conditions representative of the late 1990s, as listed in Table 2. The UA-ICON(NWP) simulations use repeated, seasonally varying climatological (1979–2016) conditions for the sea-surface temperatures and sea-ice concentrations from the Program for Climate Model Diagnosis and Intercomparison (PCMDI) Atmospheric Model Intercomparison Project (PCMDI-AMIP 1.1.2) dataset (Taylor et al., 2000). The radiatively active gases in ecRAD are prescribed as globally yearly averaged values (1990-2000) for CO_2, and modified with a $\tanh$ profile for CH_4, N_2O, CFC-11, and CFC-12. Tropospheric background aerosol optical properties, representing conditions of the year 1865, are prescribed for ecRAD (Kinne et al., 2013). The radiatively active gases for the upper-atmosphere extension, namely CO_2, NO, O_3, O_2, and O, and the O_3 for ecRad are prescribed from a 35-year climatology of a HAMMONIA simulation (Schmidt et al., 2006). The solar forcing is constant with 14 spectrally resolved irradiances and a total solar irradiance of 1361.12 W m^{-2}, averaged from 1979–2016, using the dataset prepared for CMIP6 (Matthes et al., 2017); the F10.7 cm solar flux for the calculation of the EUV heating rates is set to 150 sfu (1 sfu = 1×10^{-22} W m^{-2} Hz^{-1}). The 20-year UA-ICON(ECHAM) simulation uses the same boundary conditions and settings as Borchert et al. (2019), the UA-ICON(NWPD),

and UA-ICON(NWP) simulations all use NWP physics. They are run for 60 years after one year of spin-up. UA-ICON with NWP physics requires longer simulation periods, than UA-ICON with ECHAM physics, e.g. for reliable conclusions concerning statistics based on major SSWs, as the dynamic variability is much larger. The second simulation, UA-ICON(NWPD), uses the default settings (therefore labelled NWPD) for the OGWD and NGWD parameterizations (Label F1C1 in Table 3) and UA-ICON(NWP) uses tuned parameters for the OGWD and NGWD parameterizations (Label F2C30-S in Table 3). The major features of ECHAM and NWP physics are summarized in Table 1. Especially the difference in NGWD parameterization between the physics packages, Hines (1997a, b) (H97) in ECHAM and Warner and McIntyre (1996) (WM96) in NWP, has a substantial impact on the climatology of the MLT, which is emphasized in Sect. 3.

Label	C^*	$\rho_0|\hat{\mathbf{F}}_p|$	K_{wake}	K_{drag}	Fr_{crit}
NoNGWD	-	-	1.5	0.075	0.4
NWPD (F1C1)	1.0	2.50	1.5	0.075	0.4
NWP (F2C30-S)	30.0	1.75	1.1	0.052	0.6

Table 3. Parameter setting of the WM96 NGWD (C^*, $\rho_0|\hat{\mathbf{F}}_p|$) and the LM97 OGWD parameterizations of the tuning simulations in perpetual January mode; C^*, a factor to increase the saturation momentum flux density; $\rho_0|\hat{\mathbf{F}}_p|$, the total launch momentum flux in each azimuth in mPa; K_{wake}, the low-level wake drag constant; K_{drag}, the gravity wave drag constant; Fr_{crit}, the critical Froude number. All simulations use the same default settings for the WM96 tunable L_p = 450 hPa, the launch height of the gravity wave spectrum. The setups NWPD and NWP are used for the UA-ICON(NWPD) and UA-ICON(NWP) simulations with a seasonal cycle.

Table 3 gives the parameter values of the GWD parametrizations for the simulations discussed here. We have increased the scaling factor of the saturation momentum flux density (C^*) of WM96, introduced by McLandress and Scinocca (2005) when comparing H97, WM96, and Alexander and Dunkerton (1999) NGWD parameterizations. The total launch momentum flux in each azimuth ($\rho|\hat{F}_p|$) is reduced from its default value of 2.50 mPa to 1.75 mPa. The adaptations for the OGWD parameterization include changes in tunable parameters, namely the low-level wake drag constant (K_{wake}), the gravity wave drag constant (K_{drag}), and the critical Froude number (Fr_{crit}).

2.2 Reanalyses and satellite observations

We use temperature and zonal wind of the three reanalyses ERA-5 (Hersbach et al., 2020), NCEP/NCAR (Kalnay et al., 1996; Kistler et al., 2001), and MERRA2 (Gelaro et al., 2017) for the evaluation of the NH stratospheric variability and the statistical evaluation of SSWs.

For the evaluation of the MLT temperature and zonal wind, we use the latest version (v2.07, v2.08 from December 2020 onward) of satellite observations from the SABER (Sounding of the Atmosphere using Broadband Emission Radiometry) instrument on the TIMED (Thermosphere, Ionosphere, Mesosphere, Energetics and Dynamics) satellite (Russell III et al., 1999; Dawkins et al., 2018). The original level 2A data, sorted by event and altitude, is binned to a regular latitude-by-altitude grid with a temporal resolution of one month and a spatial resolution of 5° horizontally and 1 km vertically. As a reference

155   for the zonal mean zonal wind in the MLT, we use data from the UARS (Upper Atmosphere Research Satellite) Reference Atmosphere Project (URAP) (Swinbank and Ortland, 2003). For daily resolved temperature observations through the middle atmosphere, including the MLT region, we use Aura Microwave Limb Sounder (Aura-MLS) version 5.0 Level 3 data on pressure levels (Livesey et al., 2022).

2.3   Methods

160   The original UA-ICON output data are stored on the R2B4 triangular grid with an output frequency of six hours, instantaneously for the basic dynamical quantities. Additionally, temperature, pressure, and zonal and meridional wind components are output instantaneously at a one-hour frequency for the analyses of tidal activity. The model daily averaged tendencies of the physical parameterizations are output with a frequency of one day. These triangular output data are transferred to a regular Gaussian T63 grid with 192 longitudes and 96 latitudes, and 120 fixed geometric altitude levels, corresponding to the model

165   full height levels once the influence of the orography levels off, for the post-processing procedures. The so-called transformed Eulerian mean (TEM) quantities (Andrews and McIntyre, 1976; Andrews et al., 1987), namely the Eliassen–Palm (EP) diagnostics, which are the EP-Flux ($\mathbf{F}$) and its divergence ($\nabla \cdot \mathbf{F}$), and the meridional and vertical components of the residual mean meridional circulation (MMC) ($\overline{v}^*$, $\overline{w}^*$) are calculated on the 120 height levels of the T63-grid. We use the formulation of the hydrostatic primitive equations (HPE) on geometric coordinates (HPE(z)) of Hardiman et al. (2010) for the computation of the

170   EP diagnostics. Hardiman et al. (2010) demonstrated the large error made when calculating the EP diagnostics based on the formulation of the HPE on log-pressure coordinates HPE(ln(p)) for non-hydrostatic models formulated on geometric altitude levels. For the analysis of major sudden stratospheric warmings and the related diagnostics of mesospheric coupling, the daily UA-ICON output is vertically interpolated to a set of 53 standard pressure levels. This allows a more direct comparison with the reanalysis products and other published related benchmarks.

3   Global circulation

Shortcomings in the UA-ICON(NWPD) (with default settings) climatology of the MLT are the main motivation for a re-tuning of the NGWD and OGWD parameterizations in UA-ICON(NWP). We compare the zonal mean temperature (Fig. 1) and zonal mean zonal wind (Fig. 2) in the boreal and austral winter seasons from UA-ICON to SABER and URAP climatologies. Comparing UA-ICON(NWP) with its default parameter settings for the GW parameterizations, chosen for the standard version

180   up to ~75 km (Fig. 1, 2, c, g, in the following abbreviated with UA-ICON(NWPD)) with temperature from SABER (Fig. 1, a, e) and the URAP zonal wind (Fig. 2, a, e), we can identify the deficits in the MLT region with a warm temperature bias in the summer mesopause region of more than 30 K and an eastward zonal mean zonal wind extending from the middle atmosphere to the lower thermosphere during the winter seasons and a westward zonal mean zonal wind during the summer seasons reversing only slightly to an eastward direction in an altitude from 100 to 110 km. We significantly reduce these deficits of UA-

185   ICON(NWPD) in the MLT region concerning the temperature, and the zonal wind with the tuned parameters for the OGWD and NGWD parameterizations of UA-ICON(NWP) (Fig. 1, 2, b, f). The temperature in the austral and boreal summer MLT
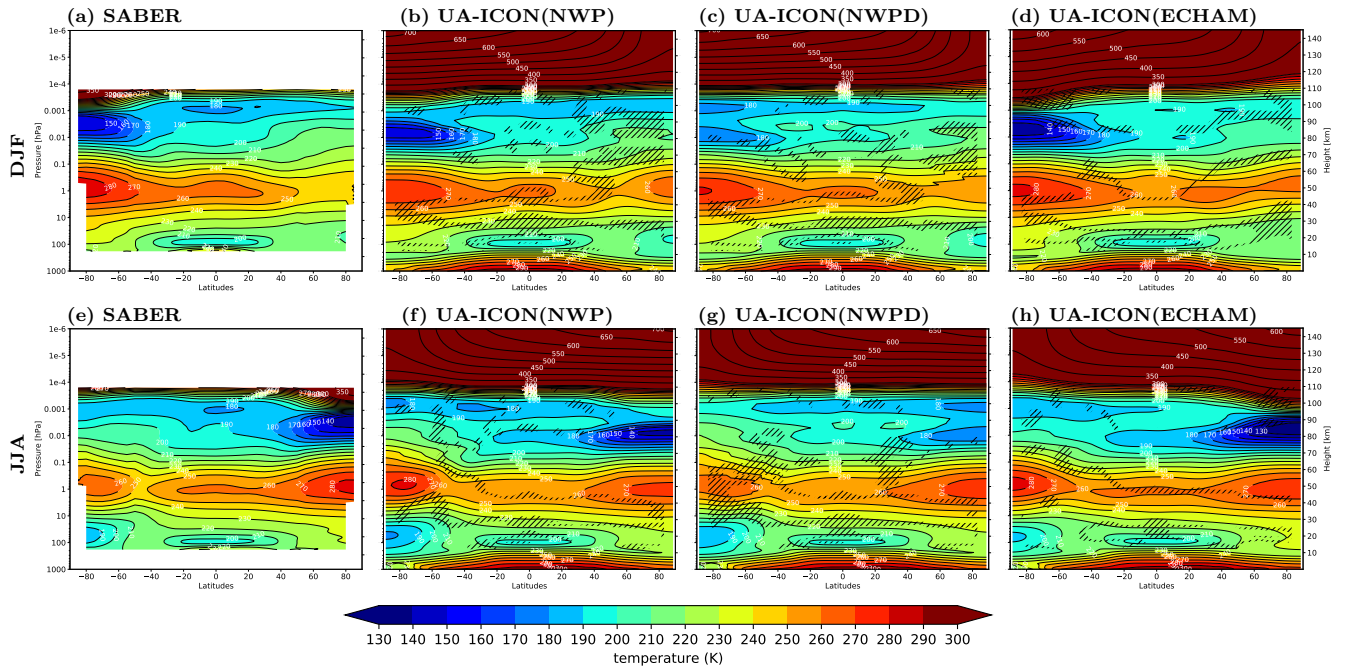
Figure 1. Climatology of zonal mean temperature for Dec./Jan./Feb. (top row a–d) and Jun./Jul./Aug. (bottom row e–h) seasonal mean; (a, e) SABER (2002–2022), (b, f) UA-ICON with NWP physics and tuned gravity waves (F2C30-S, in table 3); (c, g) UA-ICON with NWP physics (default settings, F1C1 in table 3); (d, h) UA-ICON with ECHAM physics. In the hatched areas the UA-ICON simulations are not statistically different to SABER based on the 95 % confidence level.

region is decreasing by more than 30 K in UA-ICON(NWP), now comparable to SABER (Fig. 1, a and e) during austral and boreal summer seasons, whereas UA-ICON(ECHAM) is showing a cold bias of 10 K in this region for both seasons (Fig. 1, d, h). The reversals from the westward-directed summer zonal mean zonal wind in the middle atmosphere to an eastward zonal

190   wind direction in the upper mesosphere are present in UA-ICON(NWP) (Fig. 2, b and f) with a magnitude stronger compared to URAP (Fig. 2, a and e), whereas UA-ICON(ECHAM) (Fig. 2, d and h) shows a wind reversal too intense and too low in altitude as reported by Borchert et al. (2019). This effect of the NGWD tuning in UA-ICON(NWP) limits the mesospheric polar vortex to an altitude of ~80 km, whereas in both winter seasons, it extends to an altitude of approximately 100 km in the URAP climatology. Comparable differences were reported, e.g., by Harvey et al. (2019) in modelling the extension of the mesospheric

195   polar vortex with WACCM, although specifying the dynamics up to 60 km from MERRA2 data. The winter westerly winds at high latitudes in WACCM extend to lower altitudes, compared to geostrophic zonal winds calculated from SABER-derived geopotential heights. The magnitude of the eastward-directed zonal winter circulation in the middle atmosphere is too high in the SH in UA-ICON(NWP) by 20 m s^{-1}, and slightly too high in the NH. However, the position of the westerly jets is well captured in both hemispheres compared to URAP. A second side effect of increasing the eastward-directed NGWD in

200   UA-ICON(NWP) is the weakening of the westward-directed zonal circulation in summer, leading to a shift of the -30 m s^{-1}
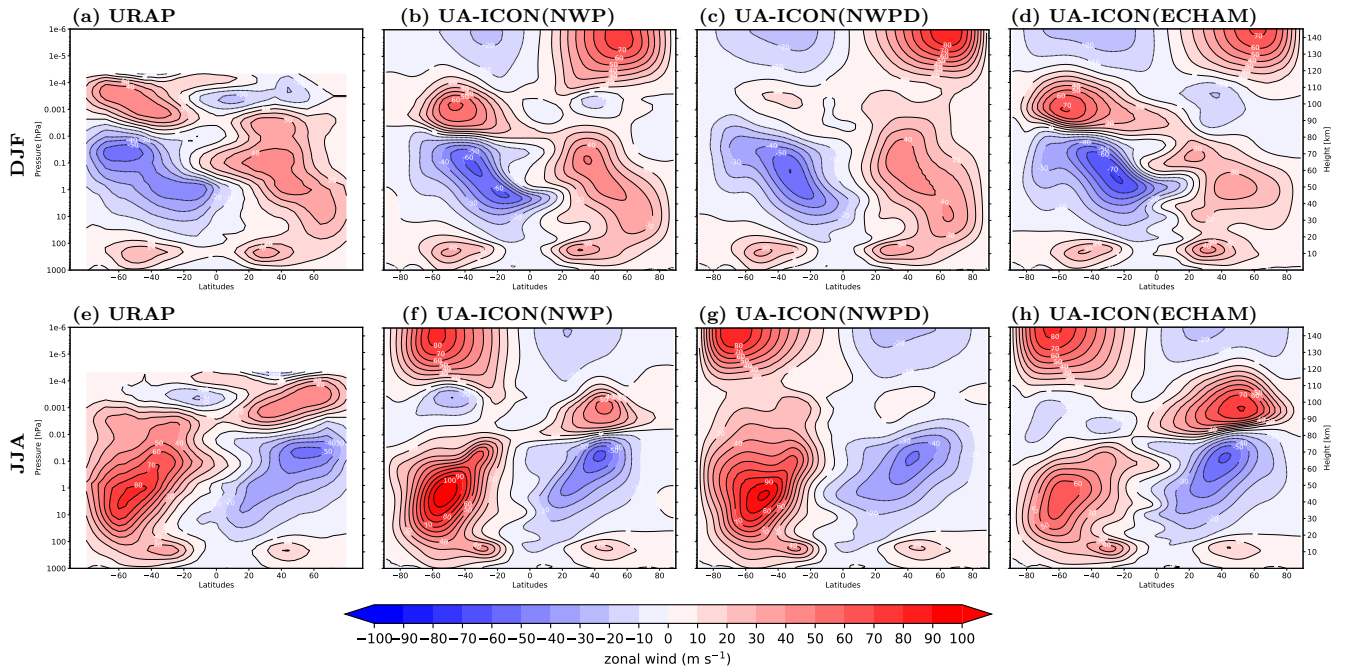
Figure 2. Climatology of zonal mean zonal wind for Dec./Jan./Feb. (top row a–d) and Jun./Jul./Aug. (bottom row e–h) seasonal mean; (a, e) URAP climatology; (b, f) UA-ICON with NWP physics and tuned gravity waves (F2C30-S, in table 3); (c, g) UA-ICON with NWP physics (default settings, F1C1 in table 3); (d, h) UA-ICON with ECHAM physics.

contour to lower latitudes by more than $10°$ in the upper mesosphere. The magnitude of the NH summer westward-directed zonal circulation ($<$-50 m s^{-1}) compares well with URAP, however, the location of this easterly jet is too low in altitude and shifted too far to low latitudes. This shift of the easterly jet appears as well in the SH summer together with a slightly too strong westward-directed zonal circulation ($<$-60 m s^{-1}).

205   UA-ICON(ECHAM) and UA-ICON(NWPD) have a warm bias in winter stratopause temperature compared to SABER, which intensifies by the tuning of the NGWD parameterization in UA-ICON(NWP). However, the winter stratospheric temperature is in better agreement with SABER for both UA-ICON(NWP) and UA-ICON(NWPD), and the strength of the northern hemispheric stratospheric vortex is much better captured compared with URAP. In general, using ICON with the NWP physics package leads to a much better representation of the stratosphere that eliminates the problems with the stratospheric circulation

210   and temperatures in ICON(ECHAM) noticed by Giorgetta et al. (2018) and for UA-ICON(ECHAM) by Borchert et al. (2019). However, overall, the differences in zonal mean temperature between all UA-ICON simulations and SABER are significant in most areas, as indicated by the non-hatched areas in Fig. 1. The same holds for the zonal mean wind compared to ERA-5, where all UA-ICON simulations show significant differences in most areas up to 80 km altitude (not shown).

The main driver of the mesosphere global circulation is the breaking of NGWs (e.g., Becker, 2012; Vincent, 2015, and

215   references therein) that force a meridional circulation from the summer hemisphere to the winter hemisphere, downwelling
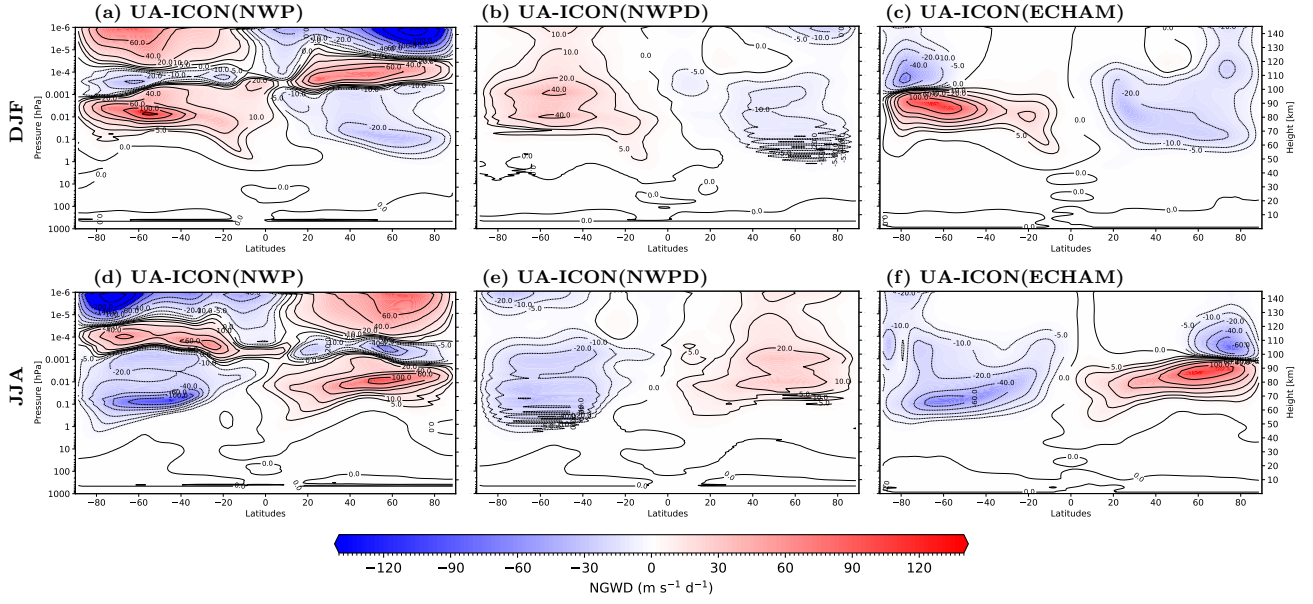
Figure 3. Multi-year boreal (top row a–c) and austral (bottom row d–f) winter seasonal, zonal mean zonal wind tendencies in m s^{-1} d^{-1} due to non-orographic gravity waves of UA-ICON simulations with NWP physics (Warner and McIntyre, 1996) with tuned gravity waves (a, d), NWP physics with default gravity wave parameters (b, e), and ECHAM physics (Hines, 1997a, b) (c, f).
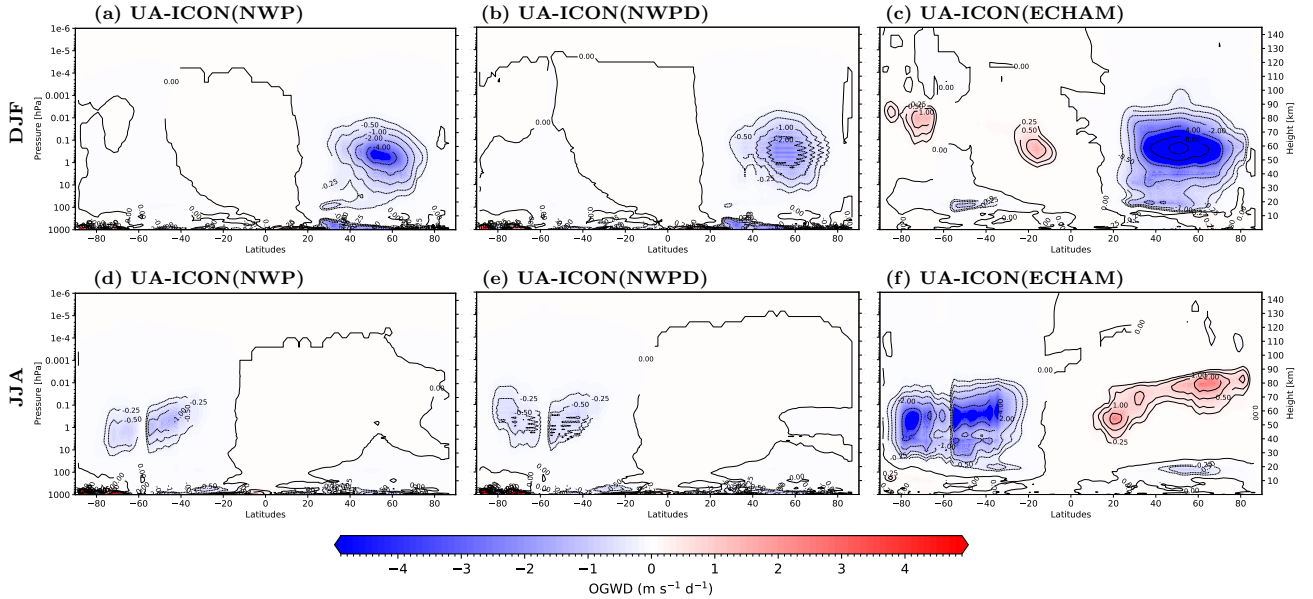
Figure 4. Multi-year boreal (top row a–c) and austral (bottom row d–f) winter seasonal, zonal mean zonal wind tendencies in m s^{-1} d^{-1} due to orographic gravity waves of UA-ICON simulations with NWP physics (Lott and Miller, 1997) with tuned non-orographic gravity waves (a, d), NWP physics with default gravity wave parameters (b, e), and ECHAM physics (Lott, 1999) (c, f).

and adiabatic warming over the winter pole, and in turn upwelling in the summer mesosphere leading to adiabatic cooling with temperatures far below the radiative equilibrium. The coarse resolution of the UA-ICON simulations in the present work does not allow for explicitly resolving the upward propagation and breaking of NGWs. Therefore, the effects of NGWs are parameterized according to H97 in UA-ICON(ECHAM) and based on WM96 in UA-ICON(NWP). Figure 3 shows the zonal

220   mean zonal wind tendencies due to the parameterized NGWD. Compared to the H97 tuning, with more than 130 m s^{-1} d^{-1} in both winter seasons in an altitude between 80 and 100 km (Fig. 3, c, f), WM96, with NWP default settings, shows much smaller tendencies only up to 40 m s^{-1} d^{-1} in SH winter or 24 m s^{-1} d^{-1} in NH winter (Fig. 3, b, e). This missing NGWD in the MLT is mainly responsible for the large discrepancies in climatological zonal mean zonal wind and temperatures as present in UA-ICON(NWPD) (Fig. 2, 1, c, g) and by increasing the NGWD of WM96 in the MLT to values comparable to H97 (Fig. 3, a,

225   d) the temperature and zonal wind in the MLT improve considerably (Fig. 1, 2, b, f). The latitudinal structure of the zonal wind tendencies from the H97 and WM96 up to an altitude of 100 km are very similar. This similarity is the result of increasing the saturation momentum flux density of WM96, as proposed by McLandress and Scinocca (2005) by a factor of 30 (see Sect. 4 for more details). Both physics packages in ICON use the parameterization based on Lott and Miller (1997) (LM97) to account for the OGWD. However, the ECHAM physics package uses the implementation of ECHAM6 (Lott, 1999), whereas NWP

230   physics uses the COSMO implementation. OGWD is acting mainly in the stratosphere, and the resulting zonal mean zonal wind tendencies show relatively huge differences of up to a factor of four, with larger OGWD in UA-ICON(ECHAM) (Fig. 4, c, f) than in UA-ICON(NWPD) (Fig. 4, b, e) and UA-ICON(NWP) (Fig. 4, a, d). The parameters of the OGWD parameterization in UA-ICON(NWP) are adapted for the coarser R2B4 horizontal resolution of UA-ICON as listed in Table 3 (F2C30-S). By this, the OGWD increases in the NH middle atmosphere in winter by a factor of two (UA-ICON(NWP), Fig. 4, a), whereas there

235   are only minor changes in JJA (Fig. 4, d).

4   Gravity wave tuning

The tuning parameters applied in the UA-ICON(NWP) simulation are the result of a series of perpetual January simulations (supplement Table 1) with variations of C* of WM96. The total launch momentum flux in each azimuth ($\rho|\hat{F}_p|$) is tested with its default value of 2.50 mPa and compared with 1.75 mPa, and the launch height (L$_p$ = 450 hPa) stays with its default value.

240   The simulation NWP includes changes in tunable parameters of the OGWD parameterization. Detailed results of these tuning simulations are documented in the supplement to this paper. Table 3 gives a subset of these simulations discussed here, with focus on the effects of switching off the WM96 NGWD completely (NoNGWD) and the final changes in the parameter settings of the WM96 and LM97 parameterizations (NWP), compared to the default settings (NWPD) (Fig. 5).

   By switching off the WM96 NGWD completely (NoNGWD), we can evaluate the effect of the parameterized NGWs, shown

245   with the latitude-altitude sections (Fig. 5) of the anomalies NoNGWD minus NWPD (left column). NoNGWD shows a strong response for all quantities, with the summer mesopause being too high in altitude and temperatures lower than the default (NWPD) case. The SH easterly wind regime extends to the lower thermosphere, and the meridional component of the residual MMC ($\overline{v}^*$), the northward directed summer to winter circulation, is more intense and shifted to higher altitudes, peaking

between 100–120 km globally. The EP-flux divergence ($\nabla \cdot \mathbf{F}$) reflects the forcing of the zonal mean zonal wind by resolved waves. The simulation NoNGWD shows $\nabla \cdot \mathbf{F}$ more intense and in the opposite direction than NWPD, indicating an increase in dissipating resolved waves. These are the resolved waves with an eastward-directed phase speed, which can propagate to considerably higher altitudes in the easterly wind regime extending to the MLT region in the SH. The simulation NWP, with an increasing C^* and a smaller $\rho|\hat{F}_p|$, shows better results in the MLT. The parameterized WM96 NGWD increases by increasing the saturated momentum flux density from its default $C^* = 1$ to $C^* = 30$, which effectively increases the altitude where the upward propagating NGWs dissipate with a direct impact on the tendency of the zonal wind in the MLT region calculated by the NGWD parameterization (NGWD, Fig. 5, d). The anomalies indicate an increase of the weak eastward-directed NGWD of 40 m s^{-1} d^{-1} in the SH of the default (NWPD, Fig. 5(d), left and Fig. 3(b)) by 100 m s^{-1} to 140 m s^{-1} (NWP, Fig. 5(d), right and Fig. 3(a)) within a shallow layer, peaking near 81 km. Near 100 km, the NGWD changes to a westward direction in NWP in a layer up to about 120 km and turns again to an eastward direction. Increasing the eastward-directed NGWD in the SH upper mesosphere accelerates the zonal mean zonal wind in the SH MLT by more than 50 m s^{-1} (Fig. 5(b), right), and intensifies the MMC, as indicated by the stronger northward-directed summer-to-winter $\overline{v}^*$ near 80 km altitude (Fig. 5(c), right). The forced up-welling in high latitudes in the SH leads to adiabatic cooling in the MLT, peaking with -50 K in a layer from 80 to 90 km (Fig. 5(a), right). Above 100 km the MMC turns to a southward-directed flow with increasing C^*, which is directly related to the more westward-directed NGWD-induced zonal wind changes in the SH and the change to an eastward-directed NGWD in the NH. This winter-to-summer directed flow extends over both hemispheres in a layer between 100 and 120 km with a minimum near the Equator. Qian et al. (2017) and Wang et al. (2022) reported similar features for SD-WACCM simulations and compared them to the MMC derived from vertical gradients of SABER CO_2 volume mixing ratio. They found large vertical CO_2 gradients in the 95–110 km height region at summer hemispheric polar latitudes consistent with the SD-WACCM CO_2 gradients, and the upward-directed residual flow in the upper mesosphere and the downward-directed residual flow of the lower thermosphere.

The significant NGWD changes in the NH contribute to decelerating the eastward-directed polar night jet in the upper mesosphere, whereas the zonal wind changes around the stratopause are due to more intense westward-directed OGWD (see Fig. 4, a, b).

Derived from the numerical experiments, one parameter setup, NWP (F2C30-S), in Table 3 corresponding to $C^* = 30$ and an adaptation of the OGWD parameters, provides the most reasonable prediction and therefore is used for further investigations in the time slice simulation UA-ICON(NWP) in Table 2. This version best reproduces a reasonably strong westerly stratospheric jet and an easterly mesospheric jet in the northern hemisphere and their reversed counterparts in the southern hemisphere, as well as a reasonably low temperature in the summer mesopause region.

5 Northern hemisphere stratospheric and mesospheric winter variability

The process of parameter optimization (tuning), presented in Sect. 4 has been done with a clear focus on the climatological state of the MLT, where the parameter optimized simulation UA-ICON(NWP) shows a clear improvement. However, parameter
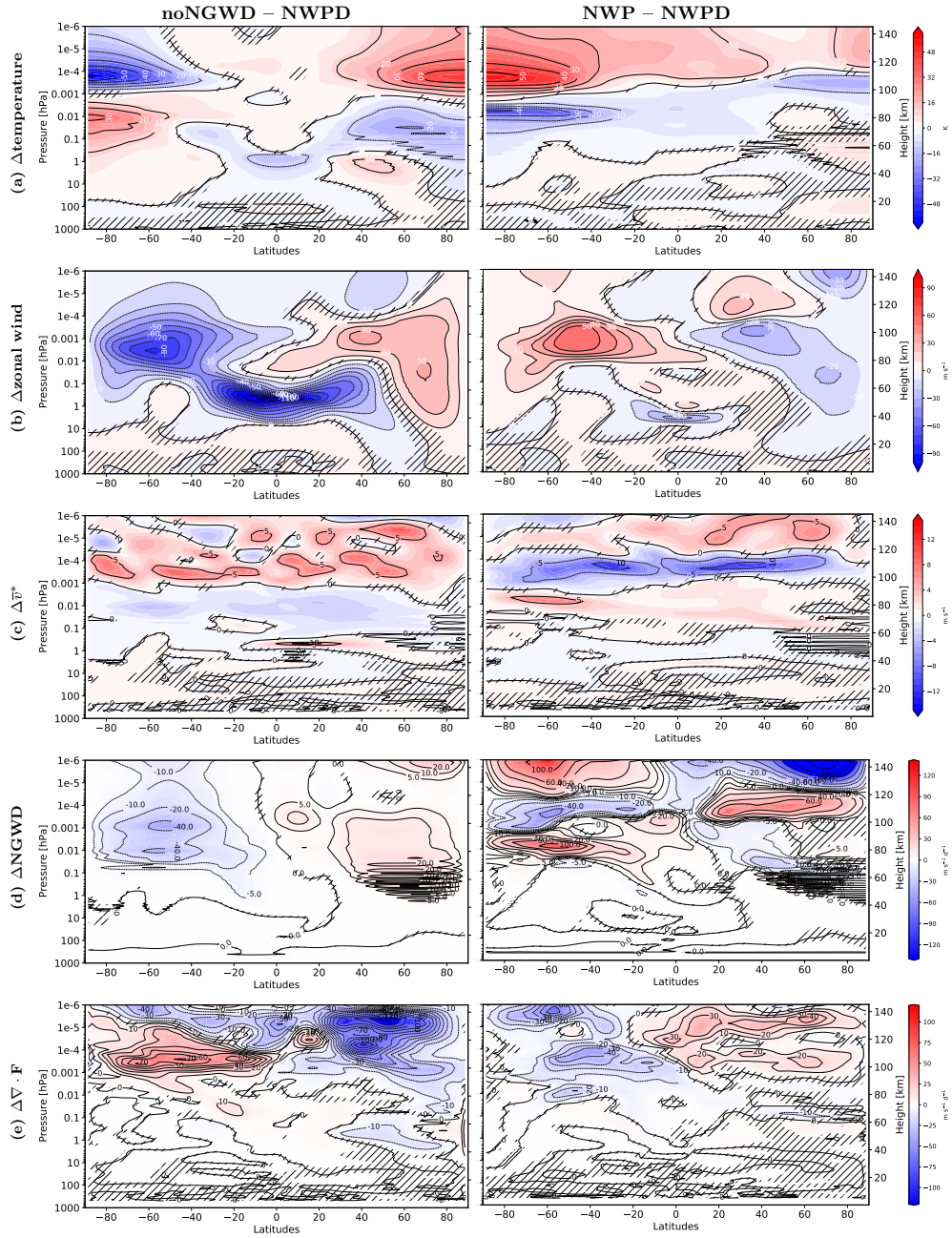
Figure 5. Perpetual January zonal mean long-term mean anomalies calculated with respect to NWPD (F1C1) for noNGWD (left row) and NWP (F2C30-S) (right row); (a) temperature in K; (b) zonal wind in m s^{-1}; (c) transformed Eulerian mean meridional velocity ($\overline{v}^*$) in m s^{-1}; (d) zonal wind tendency due to non-orographic gravity waves in m s^{-1} d^{-1}; (e) divergence of the Eliassen-Palm vector ($\nabla \cdot \mathbf{F}$) in m s^{-1} d^{-1}. In the hatched areas the anomalies are not statistically significant, based on the 95 % confidence level.

optimizations otherwise potentially worsen the model performance in other regions of the atmosphere, e.g. as discussed for the warm stratopause temperature bias. In this section, we focus on the NH stratospheric and mesospheric winter variability, to evaluate the implication of the parameter optimization on this important dynamical aspect of the model. A key measure for the NH winter variability is the frequency of major SSWs, strongly related to troposphere-stratosphere coupling via the upward propagation of planetary wave and gravity wave activity (Sect. 5.2).

5.1 Seasonal cycle of northern hemisphere stratospheric variability

(a) Daily 10 hPa temperature near the North pole

(b) Daily 10 hPa zonal mean zonal wind near 60°N
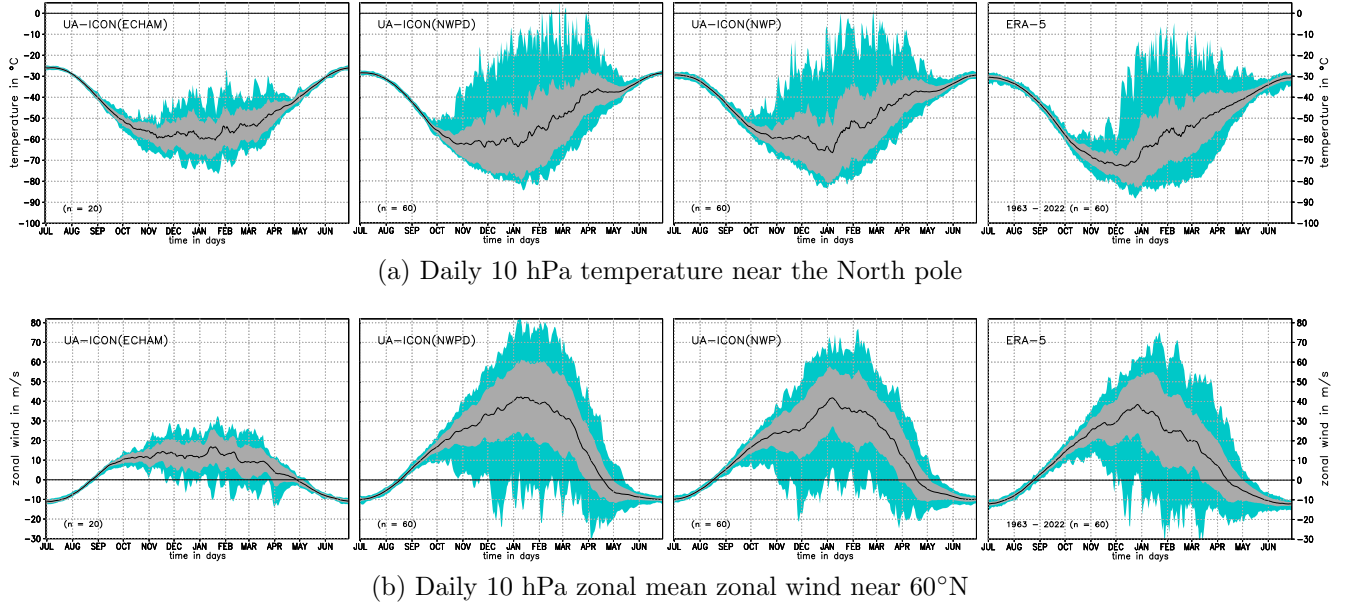
Figure 6. Climatological seasonal cycle of daily 10 hPa temperature near the North pole; (b) zonal mean zonal wind near 60°N for UA-ICON simulations and ERA-5. From left to right: UA-ICON(ECHAM), UA-ICON(NWPD), UA-ICON(NWP), and ERA-5 (1963–2022). The black solid line indicates long-term averaged daily mean time series; darker shading indicates a range of ±1 standard deviation around the average; lighter shading indicates the maxima/minima reached within the complete daily data sets.

Figure 6 shows the climatological seasonal cycle of NH stratospheric (10 hPa) polar temperature and mid-latitude (near 60°N) zonal wind for UA-ICON(ECHAM), UA-ICON(NWPD), UA-ICON(NWP), and ERA-5 (1963–2022) with the black solid line. Overlaid with lighter shading are the daily mean maxima and minima occurring within the 60 years (20 years for UA-ICON(ECHAM)) in each dataset. The overlaid darker shading gives the ±1 range of the standard deviation about the daily averaged time series. Figure 7 shows the deviations of the climatological seasonal cycles presented in Fig. 6 for the UA-ICON simulations compared to ERA-5. We start with a discussion of the daily climatological time series (black solid line in Fig. 6) and the deviations of the UA-ICON simulations to ERA-5 (Fig. 7). The summer temperatures are too warm by ∼4 K for UA-ICON(ECHAM), ∼1 K for UA-ICON(NWP), and by ∼2 K for UA-ICON(NWPD) compared to ERA-5. With the transition
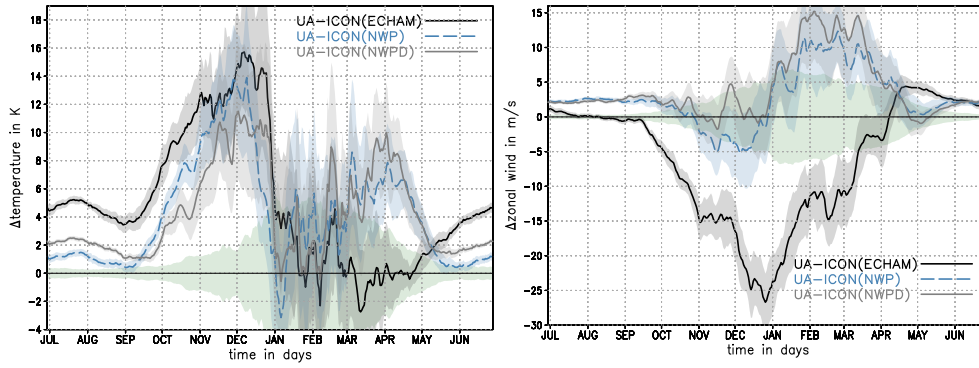
Figure 7. Climatological seasonal cycle of daily deviations of UA-ICON simulations from ERA-5; (left) 10 hPa temperature near the North pole; (right) 10 hPa zonal mean zonal wind near 60°N. The shading represents the 99% confidence interval of the individual simulations' daily mean; light green shading around the zero line indicates the 99% confidence interval of the ERA-5 data.

to the westerly circulation in October the warm biases of both UA-ICON(ECHAM) and UA-ICON(NWP) are getting larger, reaching a maximum of 11–16 K in December. The warm bias of the tuned UA-ICON(NWP) simulation is slightly larger in early winter. This larger dynamic heating is probably due to a stronger orographic GWD. Until mid to end of December, these positive anomalies are outside the 99%–confidence interval of the daily ERA-5 North Pole temperature, given with the

300   light green shading around the zero line in Fig. 7, indicating a significant warm bias in the NH polar stratosphere. On average the warm biases for the UA-ICON(NWP) and UA-ICON(ECHAM) simulations reduce in January and February fluctuating around 2–3 K, whereas UA-ICON(ECHAM) in March and April shows a good agreement with ERA-5, the warm bias of the UA-ICON(NWP) increases. The good agreement of the UA-ICON(ECHAM) simulation in 10 hPa NH polar temperatures from January to April with ERA-5 is partly a consequence of the weak intensity of the SSWs in this simulation, as seen in

305   the weak variability. Both ERA-5 and the UA-ICON(NWP) simulations show intense increases in polar 10 hPa temperature during SSWs, especially in the late winter period, contributing to an increase in the climatological mean. The 10 hPa zonal mean zonal wind near 60°N is slightly too strong for UA-ICON(NWP) simulations during the summer season, whereas UA-ICON(ECHAM) at least from late July to the beginning of September is very close to ERA-5. However, beginning with the transition to the westerly circulation UA-ICON(ECHAM) shows weak zonal winds with deviations to ERA-5 peaking at -25

310   m s^{-1} in late December. All UA-ICON(NWP) are in better agreement with ERA-5 during the NH winter season. Both UA-ICON(NWP) simulations show in October to December moderate deviations of the zonal mean zonal wind to ERA-5, most of the time within or close to the ERA-5 confidence interval. Later in winter from January to March, the zonal wind of UA-ICON(NWPD) exceeds the zonal wind in ERA-5 by up to 15 m s^{-1}, and by 5–12 m s^{-1} for UA-ICON(NWP), most of the time outside the ERA-5 confidence interval. Concerning the winter variability, presented with the daily extremes and the range of $\pm$

315   one standard deviation in Fig. 6, all UA-ICON(NWP) simulations show a far better performance than UA-ICON(ECHAM). The observational record of the NH stratospheric winter variability, given with the ERA-5 reanalysis (Fig. 6a, b, right), indicates an increase in temperature maxima near the North Pole in December. This is accompanied by the occurrence of easterly

extremes which indicate major SSW events. SSWs tend to be more intense and occur more often during January and February, as reflected by the warmest maxima and the most intense easterlies in these months. The UA-ICON(ECHAM) (Fig. 6a, b, left) simulation shows a much lower NH stratospheric winter variability, characterized by the smaller standard deviations of the wind and the temperature difference and the less pronounced extreme values, compared to the UA-ICON(NWPD) and UA-ICON(NWP) simulations. However, due to the weak zonal mean wind easterly winds occur and the criteria for SSWs are fulfilled frequently. In both UA-ICON(NWP) simulations, the range of maxima/minima is comparable to ERA-5. Concerning the timing of the most extreme temperature and zonal wind anomalies, both UA-ICON(NWP) simulations show SSW-related extremes too early in November and too late in March, however, less easterly extremes in mid-winter, than ERA-5.

5.2 Major sudden stratospheric warmings

Major SSWs are accompanied by changing mesospheric and thermospheric propagation conditions for large-scale Rossby and gravity waves, and tides. The mechanism is further illustrated in Fig. 8 with the time-height section of the averaged daily evolution of area-weighted averaged quantities centred at day zero for SSW events detected in UA-ICON(NWP). Figure 8 (left) shows the absolute values of the quantities whereas the right column shows the respective anomalies to the long-term daily mean. The zonal mean zonal wind (averaged from 50–70° N) (Fig. 8c, d) is decelerated in the stratosphere by Rossby waves with westward propagating intrinsic phase speed, focusing on the polar cap as represented by the strong convergence of the Eliassen-Palm (EP) flux $\nabla \cdot \mathbf{F}$ (averaged from 70–90° N) (Fig. 8e, f) before day zero of the SSWs exerting a strong westward directed drag on the zonal flow. The usual eastward-directed stratospheric flow allows the upward propagation of westward propagating NGWs and OGWs, creating a westward-directed drag in the stratosphere/lower mesosphere (OGWD) and mesosphere (NGWD) as shown with the polar cap (70–90° N) averaged NGWD (Fig. 8g, h) and OGWD (Fig. 8i, j). With the onset of the westward-directed flow in the stratosphere, the filter conditions for the upward propagating waves change and the Rossby waves and westward propagating gravity waves are blocked, while eastward propagating NGWs are now in favour of propagating upward. This is illustrated by the average time evolution of the wave drags around day zero of SSWs in Fig. 8. A strong increase in negative $\nabla \cdot \mathbf{F}$ (convergence) starts some days before day zero in the upper stratosphere and propagates downward. The EP-flux diagnostic $\nabla \cdot \mathbf{F}$ not only accounts for large-scale planetary waves but also includes the other scales of the model related to resolved gravity waves, e.g. the westward-directed drag emerging in the upper stratosphere/lower mesosphere after day zero. Westward-directed (negative) planetary wave drag up to 100km has been found in several model simulations (Zülicke and Becker, 2013; Limpasuvan et al., 2016; Okui et al., 2021) as a result of baroclinic/barotropic instability (Sato and Nomoto, 2015). The persistent positive $\nabla \cdot \mathbf{F}$ (divergence) in the lower thermosphere near 110 km before and after the SSWs is related to eastward propagating resolved waves. The reason for the appearance in a focussed layer around 110 km in UA-ICON is most likely in the particular vertical structure of incorporated WM96 NGWD parameterization. The westward-directed NGWD and OGWD decrease towards day zero. In the case of the NGWD, it turns eastward-directed, starting in the upper mesosphere near day zero and propagating downward near 10 hPa within 45 days. These strong changes in the wave forcing associated with SSWs have a large impact on the residual circulation as shown by the polar cap (70–90° N) average of the meridional (Fig. 8k, l, $\overline{v^*}$) and vertical (Fig. 8m, n, $\overline{w^*}$) components of the residual MMC. On average during NH
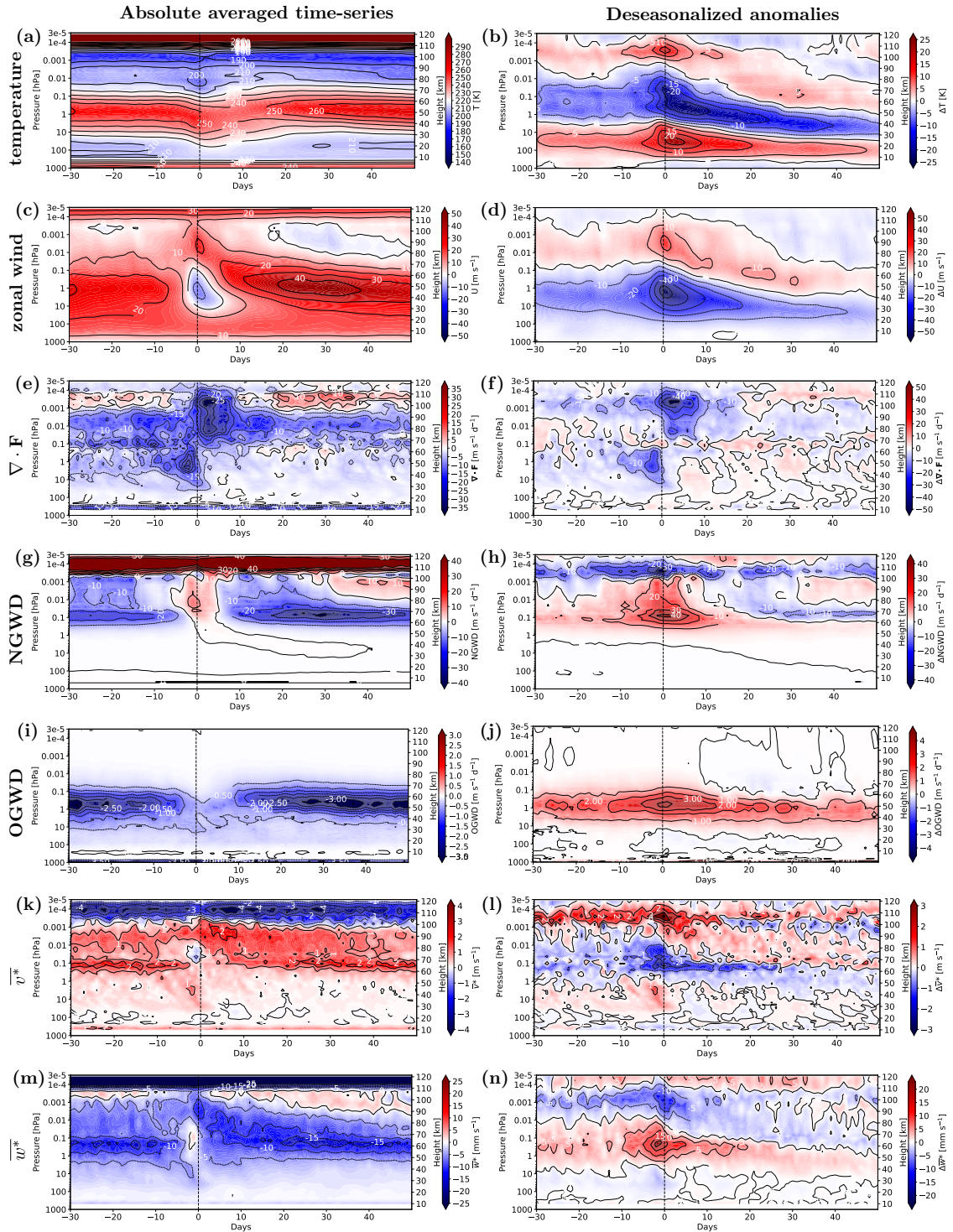
Figure 8. Time-height section of the UA-ICON(NWP) daily evolution of averaged quantities in a period around SSW events (left); associated anomalies of the averaged quantities relative to the respective long-term daily mean (right). At day zero (the central day, vertical dashed line) the WMO criterion at 10 hPa for major SSWs is fulfilled for the first time.

winter conditions $\overline{v^*}$ is northward directed (positive) and strongest in the lower mesosphere (60–70 km). In the course of SSW events, the mesospheric northward-directed $\overline{v^*}$ weakens or even reverses to a southward-directed (negative) flow whereas the northward-directed $\overline{v^*}$ intensifies in the stratosphere. Consistently, for continuity reasons, the average NH winter conditions of down-welling (negative $\overline{w^*}$) in the stratosphere and mesosphere change to an upward-directed flow in the lower mesosphere and an intensification of the down-welling in the stratosphere. The related anomalies of $\overline{v^*}$ and $\overline{w^*}$ (Fig. 8l, n) emphasize the outlined SSW-related changes in the residual MMC which are directly related to the induced adiabatic temperature changes with strong warming in the stratosphere, a strong cooling in the mesosphere, and again warming in the lower thermosphere (Fig. 8a, b).

For detecting major SSWs, we apply the so-called WMO criterion (Mcinturff, 1978; Labitzke, 1981). According to this, two conditions need to be met at a pressure level of 10 hPa, reversing the climatological winter conditions in the middle stratosphere, (I) the zonal average zonal wind at 60°N ($\overline{U}_{60N}$) has to be in a westward direction (easterly wind), and (II) the difference in temperature between the zonal average at 60°N and the North Pole ($\overline{\Delta T}$) has to be positive within a time window of ±5 days around the central date of the SSW which is the first day when condition I is fulfilled. The detection algorithm requires at least 20 days of westerly $\overline{U}_{60N}$ between two SSWs and preceding an SSW at least 10 days of westerlies with at least one day exceeding the threshold of 5 m s^{-1}. With these additional constraints, we prevent counting one SSW twice and distinguish final warmings from SSWs. Charlton and Polvani (2007) introduced the 20 days, based on the calculation of thermal damping times by Newman and Rosenfield (1997), a period that approximates two radiative time scales at 10 hPa.

There is substantial variability in the number of SSWs detected per decade (Fig. 9a), and the SSW frequency reported in the literature is therefore dependent on the analysis period, in addition to the criterion applied for the SSW detection (Butler et al., 2015). The value of 6 SSWs per decade, frequently reported (e.g. Charlton and Polvani, 2007; Butler et al., 2017), refers to SSW detection based on the 10 hPa $\overline{U}_{60N}$ only, as introduced by Charlton and Polvani (2007). The WMO criterion applied in this study gives slightly lower SSW frequencies (∼4.8–5.8 SSWs/decade) for the reanalyses, as it is more strict by additionally taking into account the $\overline{\Delta T}$ condition. Figure 9 shows the statistical evaluation of SSWs in the UA-ICON simulations in comparison to reanalyses from NCEP/NCAR (1963–2022), ERA-5 (1963–2022), and MERRA2 (1980–2022). The SSW frequency and additional SSW statistics characterizing major SSWs on average are summarized in Tables 4 and 5 for the UA-ICON time slice simulations and the reanalyses (Zülicke et al., 2018). These are in Table 4 the SSW frequency per decade (F$_{SSW}$), the event duration in days (D), the maximum 10 hPa, 60° N easterly zonal mean zonal wind speed within an event in m s^{-1} (E$_{max}$), the event accumulated easterlies in m s^{-1} (I$_{acc}$).

The time series of the 10-year moving averaged SSW frequencies (Fig. 9a) exhibit large variations for the reanalyses and the UA-ICON(NWP) simulations, whereas the variations for the UA-ICON(ECHAM) simulations are relatively small. The drop to zero for the reanalyses at year 26 corresponds to the 10 years of SSW absence observed from 1988 to 1997, which incidentally is reproduced by UA-ICON(NWPD). Stratospheric variability and the variations in SSW frequency of the observational record have been attributed to several forcing mechanisms acting from above, such as solar variability (Labitzke, 1987), propagating upward from the troposphere as planetary wave variations related to, e.g. variability of SST, for example, ENSO activity (Sassi et al., 2004; Manzini et al., 2006; Domeisen et al., 2019), variations in the Eurasian snow cover (Cohen et al., 2007;
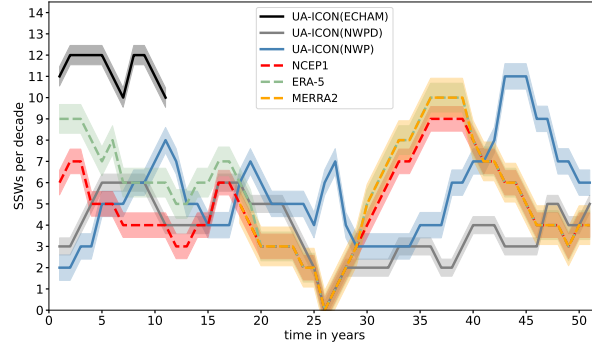
(a) 10-years moving average SSW frequency
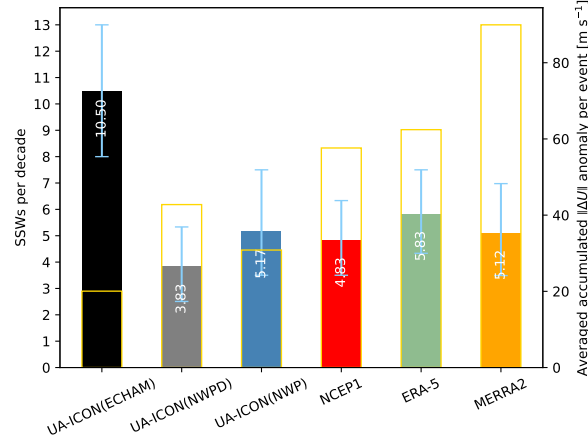
(b) Winter season, November–March
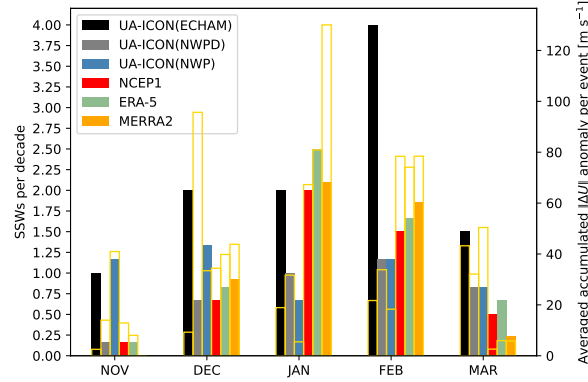
(c) Monthly distribution

Figure 9. (a) Time series of the 10-year moving averaged major sudden stratospheric warming (SSW) frequency in events per decade within the NH winter season (November–March) for UA-ICON simulations and reanalyses; the shading indicates the 95% confidence interval. (b) Bar chart of SSWs per decade with error bars indicating the 95% confidence interval; (c) the monthly distribution of SSWs per decade. The statistics are based on a period of 20 years for UA-ICON(ECHAM), and 60 years for UA-ICON(NWPD), UA-ICON(NWP), NCEP1, ERA-5 (1963-2022), and 23 years for MERRA2 (1980-2022).

Schimanke et al., 2011), or processes of internal stratospheric variability like the Quasi-Biennial-Oscillation (QBO) (Holton and Tan, 1980). However, none of these external drivers for stratospheric variability is included in the UA-ICON simulations, and the ocean surface state is based on an average over the years 1979-2016, therefore the variations in SSW frequency are part of the intrinsic model variability. Other studies, however, emphasize the role of the stratosphere itself in acting as a wave amplifier, as discussed in de la Cámara et al. (2019). The bar charts display the number of SSWs per decade (full coloured bars) with the error bars indicating the 95% confidence interval (CI) (F_{SSW} in Table 4), derived from a bootstrapping method applied individually to the complete time series of yearly SSW frequency of each dataset and re-sampling 50,000 times, with replacement, the same number of years (the same approach as in Wu and Reichler, 2020). The open, yellow bars indicate the average intensity of the SSWs in terms of the averaged accumulated easterly wind anomalies (I_{acc} in Table 4). The frequency of SSW events during the winter season from November to March (Fig. 9a, F_{SSW} in Tab. 4) for the reanalyses are in the range of 4.8 (1.4 CI) to 5.8 (1.6 CI) per decade, given by NCEP/NCAR and ERA-5, respectively, whereas MERRA2 lies in between. Although NCEP/NCAR and ERA-5 statistics are derived for the same period, they differ by one event per decade, as some events are not captured by NCEP/NCAR, probably due to the relatively low model top in the stratosphere. MERRA2 gives a lower frequency of SSWs than ERA-5, but this is caused by the shorter period used for MERRA2, and limiting ERA-5 to 1980-2022 shows the same SSW frequency as MERRA2, whereas for NCEP/NCAR the SSW frequency for 1980-2022 is again lower (4.9 SSWs/decade). There is a decrease in F_{SSW} and an increase in I_{acc} when changing from UA-ICON(ECHAM) to UA-ICON(NWP). The high F_{SSW} in the UA-ICON(ECHAM) simulation is related to the very weak stratospheric polar vortex, leading to frequent transitions to $\overline{U}_{60N}$ easterlies and a positive $\overline{\Delta T}$ during the winter period (Fig. 6), however, the average I_{acc} is only low. When applying the NWP physics package F_{SSW} and I_{acc} improve. The UA-ICON(NWP) simulation shows F_{SSW} in the range of the reanalyses but a lower I_{acc} than ERA-5, NCEP/NCAR, and MERRA2, which shows the largest I_{acc} among the reanalyses, whereas the UA-ICON(NWPD) simulation shows a slightly lower F_{SSW} but a larger I_{acc}.

The monthly distribution of the SSW frequency (Fig. 9b) from November to March shows the largest frequency in January for all reanalyses, followed by February, December, March, and November. UA-ICON(ECHAM) (black bar) has equally large SSW frequencies in December and January, and peaks in February. The UA-ICON(NWPD) simulation (grey bar), applying the default GWD parameters, has an acceptable monthly distribution of SSW frequency with a maximum in February, but frequencies too low in mid-winter and too high in March. After optimizing the GWD parameter in the UA-ICON(NWP) simulation (blue bar), the event frequency is too high in December, November, and March, and too low in January and February. The averaged SSW intensity (I_{acc}) of UA-ICON(NWP) is comparable to the reanalyses only in December but underestimated in mid-winter and overestimated in November and March.

The UA-ICON(NWP) simulation also shows lower values, compared to the reanalyses, for other wind-based statistics like the event duration (D), the maximum easterly (E_{max}), I_{acc} (Table 4), and the fraction of intense SSW events with I_{acc} exceeding 100 m s^{-1} (R_{SI}, Table 5). Concerning these statistics, the UA-ICON(NWPD) simulation with the default GWD setting agrees better with the reanalyses. The necessary tuning of the OGWD harms this aspect of the NH stratospheric winter variability, the SSW duration, maximum and accumulated easterlies of UA-ICON(NWP) are consistently lower than the reanalyses.

Table 5 summarizes additional statistical evaluations of SSW events focusing on polar vortex geometry, SSW preconditioning, and the coupling with the mesosphere. Besides R_{SI}, these are the number and fraction of split vortex SSW events (N_{SV}, R_{SV}), the number and fraction of SSWs with mesospheric coupling (N_{MC}, R_{MC}), and the number and fraction of SSWs with zonal wavenumber-2 (W2) preconditioning (N_{W2}, R_{W2}). The classification of the polar vortex geometry is based on the method of Charlton and Polvani (2007), applying an elliptic vortex diagnostic in 21 days around day zero. For this purpose, one ellipse is fitted to the pressure field if there is one low-pressure system or two ellipses if there are two low-pressure systems. Thereby displaced (DV) and split polar vortices (SV) are distinguished. The detection of the SSWs with mesospheric coupling is based on polar cap (60–90°N) area weighted averaged temperature anomalies ($\Delta\overline{T}_{60-90N}$) at 10 and 0.01 hPa. If the 10-hPa stratospheric warming and the mesospheric cooling both exceed one standard deviation, the SSW is a mesospheric coupling event. The criterion for W2 preconditioning is based on the method of Bancalá et al. (2012) and requires the amplitude of the 50-hPa geopotential height W2 to be larger than the respective W1 by more than 100 m and the 100-hPa W2 heat flux larger than the respective W1 heat flux by more than 15 K m s^{-1} in 10 days before the SSW around the day with the largest 10-hPa $\overline{U}_{60N}$ deceleration.

We start with comparing R_{SV} in UA-ICON simulations to reanalyses and an analysis of CMIP6 models by Hall et al. (2021) who uses instead of R_{SV} the ratio of SSWs with displaced and split polar vortex (DS). To better compare our measure to the published DS, we give the DS values in Table 5 and in brackets in the text. Using the reanalyses as an observational basis, the observed relative number of split-vortex events (R_{SV}) is in a range of 50-59% (1.0–0.7) with differences to a certain degree due to the re-analysis period. All UA-ICON simulations have lower R_{SV}, where UA-ICON(ECHAM), with 33% (2.0), shows the highest R_{SV}, the UA-ICON(NWPD) simulation showing the lowest with 13% (6.7) 14-16% (6.0–5.2), and the GWD-tuned UA-ICON(NWP) showing an increase to 23% (3.4). Hall et al. (2021) analysed the representation of stratospheric polar vortex variability and SSWs in CMIP6 models in comparison to ERA-5 and ERA-Interim and found for ERA-5 (1979–2020) a displaced versus split vortex ratio (DS) of 1.5. The ERA-5 DS from our vortex geometry analysis is 0.8 (R_{SV} of 54%), indicating the detection of more split vortex SSW events with our algorithm. The multi-model mean DS of the CMIP6 models analysed in Hall et al. (2021) is 2.2, but the DS range is large from 0.9 to 9.0. The DS values of the UA-ICON simulations are in the range of the CMIP6 models with 2.0 for UA-ICON(ECHAM), 6.7 for UA-ICON(NWPD), and 3.4 for UA-ICON(NWP). The deficit of UA-ICON(NWP) in the proper simulation of planetary zonal wavenumber-2 also shows with the statistics of W2-preconditioning which give R_{W2} values in the range of only 9–13% where reanalyses show a W2-preconditioning in 24% (NCEP1) or 23% (ERA-5) of the SSWs.

Data source	T	N_{SSW}	F_{SSW}	D	E_{max}	I_{acc}
UA-ICON(ECHAM)	20	21	10.50(2.50)	6.4(1.9)	-3.6(1.3)	-20.0(11.1)
UA-ICON(NWPD)	60	23	3.83(1.50)	7.0(1.7)	-8.9(2.7)	-42.8(18.1)
UA-ICON(NWP)	60	31	5.17(1.67)	6.2(1.7)	-6.1(1.6)	-30.8(13.6)
ERA-5	60	35	5.83(1.58)	8.6(2.5)	-10.4(2.6)	-62.4(26.7)
NCEP1	60	29	4.83(1.42)	8.1(2.6)	-9.6(2.7)	-57.6(28.4)
MERRA2	43	22	5.12(1.74)	11.0(4.0)	-12.6(3.5)	-89.9(40.9)
ERA-Interim/MLS	11	6	5.45(2.73)	15.3(8.3)	-16.1(6.7)	-127.3(95.8)

Table 4. Major SSW statistics for data sources (column one) with length (T) in years; total number of major SSW events and their annual frequency (N_{SSW}, F_{SSW} in events dec^{-1}), their mean duration (D in days), maximum and accumulated easterlies (E_{max} and I_{acc} in m s^{-1}) as in Zülicke et al. (2018).

Data source	N_{SI}	R_{SI}	N_{SV}	R_{SV}	DS	N_{MC}	R_{MC}	N_{W2}	R_{W2}
UA-ICON(ECHAM)	4	0.19(0.14)	7	0.33(0.21)	2.0	16	0.76(0.19)	1	0.05(0.07)
UA-ICON(NWPD)	8	0.35(0.20)	3	0.13(0.13)	6.7	20	0.87(0.17)	2	0.09(0.11)
UA-ICON(NWP)	9	0.29(0.15)	7	0.23(0.15)	3.4	29	0.94(0.11)	4	0.13(0.11)
ERA-5	14	0.40(0.16)	19	0.54(0.17)	0.8	–	–	8	0.23(0.14)
NCEP1	11	0.38(0.17)	17	0.59(0.17)	0.7	–	–	7	0.24(0.16)
MERRA2	12	0.55(0.20)	11	0.50(0.20)	1.0	–	–	4	0.18(0.14)
ERA-Interim/MLS	3	0.50(0.33)	3	0.50(0.33)	1.0	5	0.83(0.42)	1	0.17(0.17)

Table 5. Major SSW statistics for data sources (column one) with number and fraction of intense SSWs (N_{SI}, R_{SI} in #SI/#SSW), split vortex SSWs (N_{SV}, R_{SV} in #SV/#SSW), and SSW events with mesospheric coupling (N_{MC}, R_{MC} in #MC/#SSW) as in Zülicke et al. (2018), the ratio of SSWs with displaced and split polar vortex (DS), and the number and fraction of SSWs with wave-2 preconditioning (N_{W2}, R_{W2} in #W2/#SSW).

As discussed for the averaged SSW-related quantities of UA-ICON(NWP) in Fig. 8, the intense warming of the polar cap
450   stratosphere during SSWs is the result of anomalous wave forcing, leading to adiabatic stratospheric warming, an adiabatic cooling in the mesosphere, and adiabatic warming in the thermosphere. Figure 10 shows this stratosphere-mesosphere coupling with profiles of the area-weighted averaged polar cap $\Delta\overline{T}_{60-90N}$ anomalies for a time-average over 21 days centred at the onset of individual SSWs (thin dashed lines, in blue SSWs with MC, in black without MC). The thick lines represent the averages over the individual SSWs in blue for SSWs with MC and black without MC. The red profiles represent the polar cap $\Delta\overline{T}_{60-90N}$
455   anomalies for a time average over the NH winter period from November 1 to March 31, including all years. The shaded region around the red and the blue averaged profiles represents the 95% confidence interval from a bootstrap method. The top row

of Fig. 10(a-e) shows the anomalies of the respective profiles to the long-term daily climatology with both UA-ICON(NWP) simulations during SSWs showing more intense warm stratospheric anomalies and more intense mesospheric cold anomalies than UA-ICON(ECHAM). The average intensity of the positive stratospheric $\Delta\overline{T}_{60-90N}$ in UA-ICON(NWP) ($\sim$9 K) is slightly lower than Aura-MLS ($\sim$11 K). The Aura-MLS stratospheric and mesospheric $\Delta\overline{T}_{60-90N}$ is slightly more intense for the average over MC SSWs (blue profile) which is reproduced by the UA-ICON simulation. The magnitude of mesospheric cooling associated with SSWs is well represented in the GWD-tuned UA-ICON(NWP) simulation and compares well to Aura-MLS. The bottom row of Fig. 10(f-j) shows the correlation of the respective $\overline{T}_{60-90N}$ at a pressure level of 10 hPa with all other pressure levels of the UA-ICON simulations and Aura-MLS. Throughout the NH winter period (red profile), the stratosphere
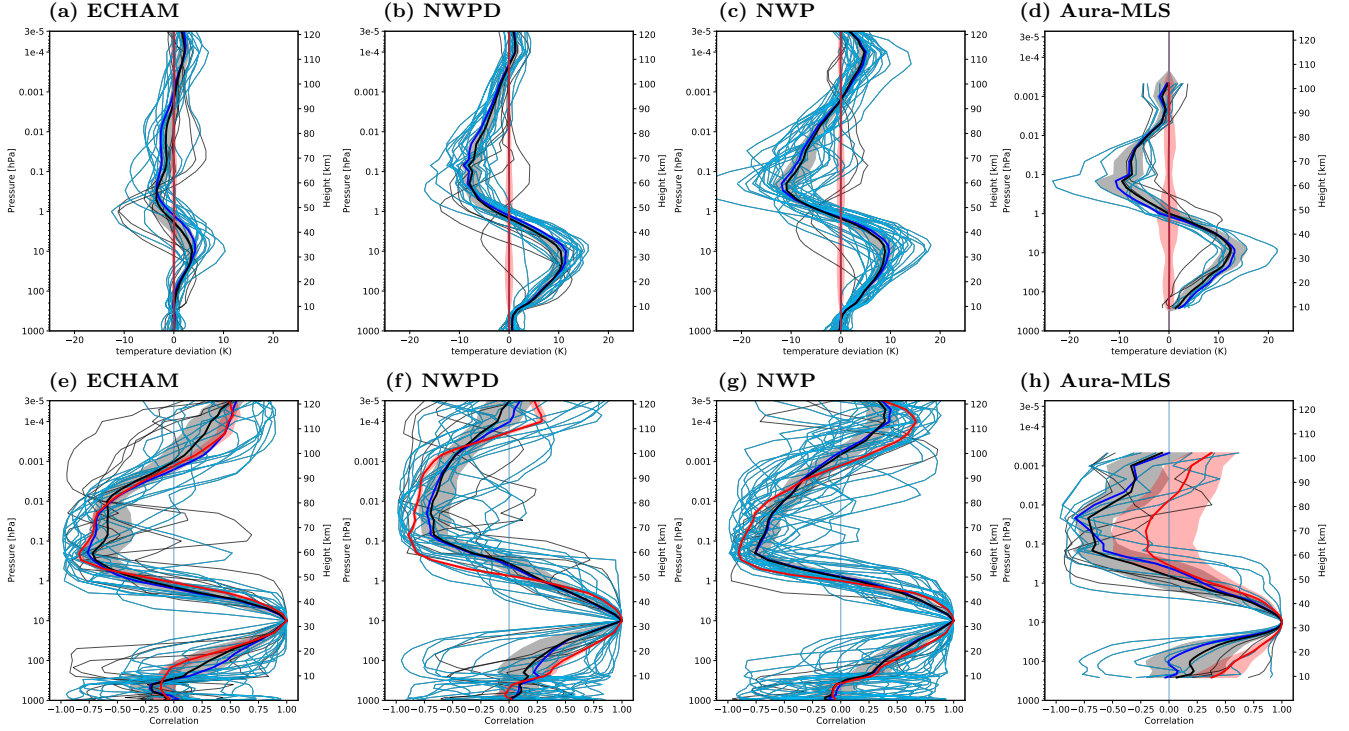
Figure 10. Top row: Vertical profiles of polar cap temperature anomalies ($\Delta\overline{T}_{60-90N}$) in 21-day windows centred at day 0 of SSWs (black and blue) or for the NH winter season from November 1 to March 31 (red) (a-e). Bottom row: Vertical profiles of correlations of $\Delta\overline{T}_{60-90N}$ in periods as above at different pressure levels with $\Delta\overline{T}_{60-90N}$ in the same period at 10 hPa (f-j). The profiles of individual SSWs are displayed with thin blue/black lines. The thick blue profile is the average of the individual SSW profiles with mesospheric coupling. The thick black line represents the average over all SSWs. The thick red profile represents the average of profiles for the complete winter season. The shaded regions give the 95% confidence intervals, estimated with a bootstrap method. The temperature anomalies are relative to the daily long-term mean. For UA-ICON simulations, (a,f) with ECHAM physics, (b,g) NWP physics default, (c,h) NWP physics and tuned GWD, (d,i) NWP physics and NWGD tuning, and (e,j) Aura-MLS.

465   is well coupled to the mesosphere, indicated by the typical anti-correlation between the stratosphere and mesosphere. The

average profile of the UA-ICON(NWPD) simulation shows the maximum anti-correlation ($\sim$-0.75) during SSWs extending over a more extended altitude region ($\sim$70–95 km) compared to UA-ICON(ECHAM) and UA-ICON(NWP), showing the largest anti-correlation vertically more focused near $\sim$75 km. By tuning the GWD parameterizations in UA-ICON(NWP) the average profile based on the entire period (thick red), in general, shows a similar behaviour with the mesospheric anti-

470 correlation focused at a lower altitude. While the vertical structure of the SSW-related anomalies in the middle atmosphere is well simulated, we find the frequency of mesospheric coupling (diagnosed with R_{MC} in Table 5) slightly too high when comparing UA-ICON(NWP) with ERA-Interim/MLS. However, it is well within the uncertainties of respective data sets and thus no matter of concern.

6 Tidal analyses

475 Figure 11 presents the amplitude of the migrating diurnal (upper eight panels) and semidiurnal (lower eight panels) tides in temperature derived from UA-ICON(NWP) and SABER as a function of latitude (50°S–50°N) and height (70–110 km). The retrieval of tides uses the least-squares technique described in Yamazaki and Siddiqui (2024). The SABER tidal climatologies are based on temperature measurements during 22 years (2002–2023), while the UA-ICON(NWP) results are based on hourly temperature outputs of 60 years. It is noted that the tidal analysis of SABER data involves a 60-day window, which might lead

480 to an underestimation of tidal amplitudes.

The latitude-altitude structure and seasonal variation of the migrating diurnal tide are well reproduced by UA-ICON(NWP). The latitude structure with the maximum temperature perturbation at the equator and secondary peaks at $\pm30°$ corresponds to the (1,1) Hough mode of classical tidal theory (Forbes, 1995). UA-ICON(NWP) also captures the semiannual variation in the amplitude of the migrating diurnal tide. That is, the amplitude is greater during the equinoxes than during the solstices. The

485 semiannual variation of the diurnal tide is well known (Burrage et al., 1995) and is generally attributed to the change in the background atmosphere, which affects the vertical propagation of the tide (McLandress, 2002a, b).

Compared to the migrating diurnal tide, the migrating semidiurnal tide has a longer vertical wavelength and thus can propagate deeper into the thermosphere (Forbes, 1995). UA-ICON(NWP) reproduces a rapid increase of the semidiurnal tidal amplitude above $\sim$95 km. The model also reproduces the seasonal variation with larger amplitudes during June and September

490 than during December and March. However, the model tends to underestimate the amplitude in all seasons.

The migrating diurnal and semidiurnal tides in the MLT region from UA-ICON(NWP) also compare well with those from other numerical models such as WACCM-X (e.g., Liu et al., 2018a) and eCMAM (e.g., Beagley et al., 2000). Like UA-ICON(NWP), both these models produce a realistic seasonal variability of migrating tides in the MLT region. However, tidal amplitudes are slightly overestimated in eCMAM (e.g., Gan et al., 2014) and underestimated in WACCM-X (e.g., Liu et al.,

495 2018b) when compared to SABER temperature observations. Tides from UA-ICON(NWP) do not differ significantly from eCMAM and WACCM-X, implying that UA-ICON(NWP) is at least as capable as both these models in producing migrating tidal variability in the MLT region close to observations.
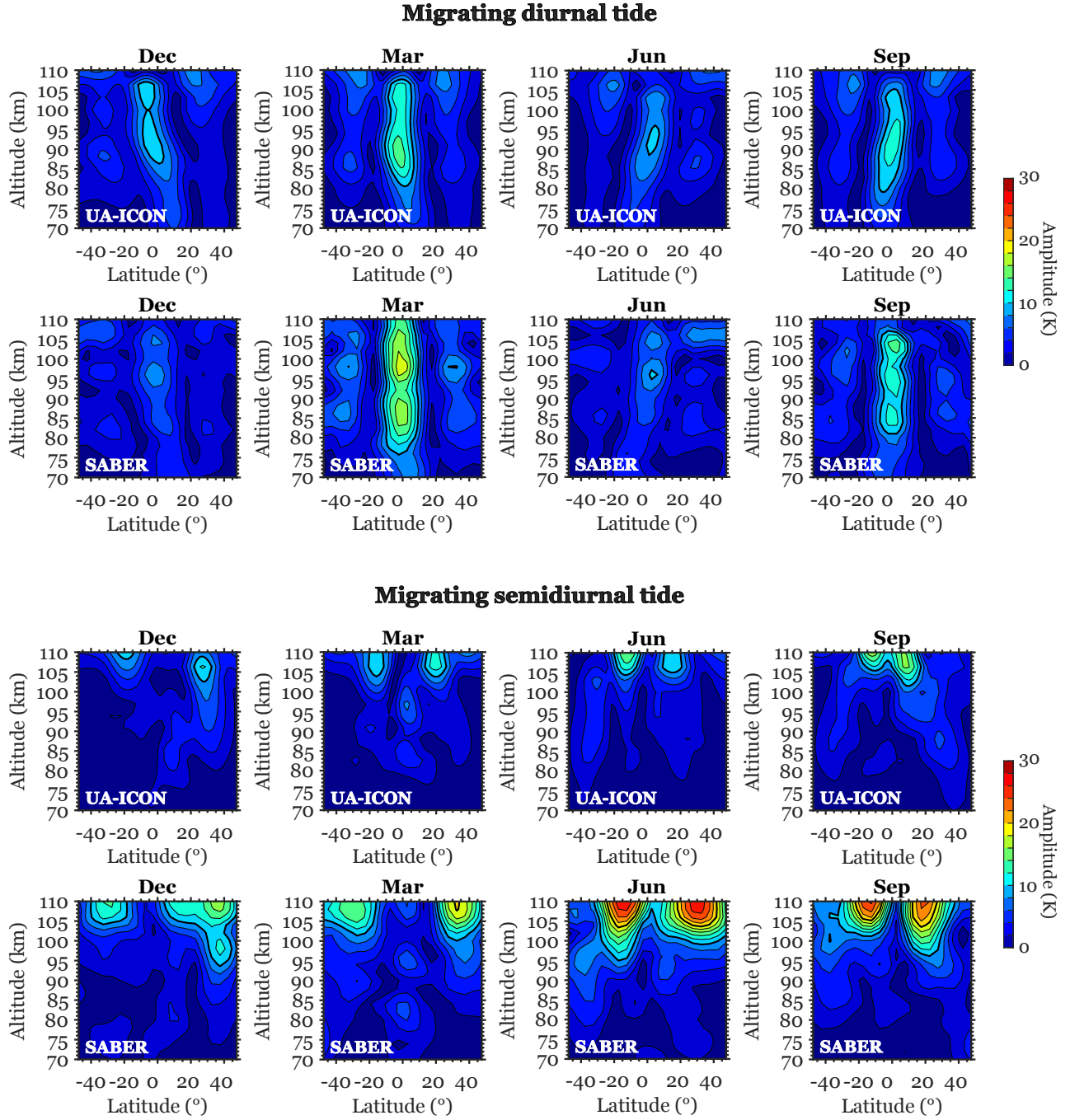
Figure 11. Amplitude of the migrating diurnal and semidiurnal tides in temperature as derived from UA-ICON(NWP) and SABER.
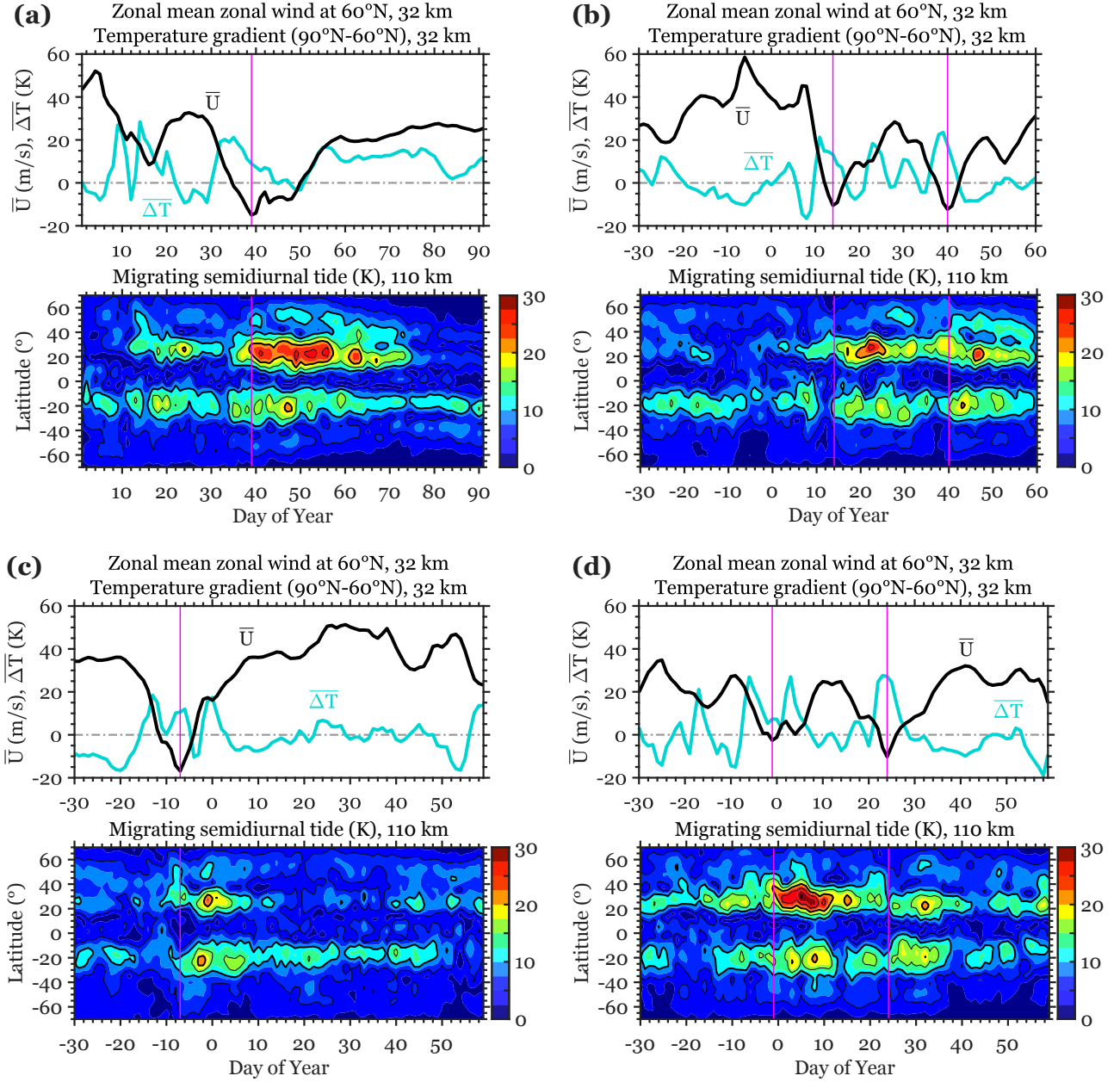
Figure 12. Amplitude of the migrating semidiurnal tide in temperature at 110 km as derived from UA-ICON(NWP) during four selected boreal winters containing major SSWs. The vertical lines correspond to the days of the peak reversal of the zonal-mean zonal wind.

We also examine the tidal variability during SSWs as simulated by UA-ICON(NWP). It is well known that tides at MLT altitudes can be significantly altered during SSWs (e.g., Pedatella et al., 2014; Siddiqui et al., 2022). Especially, an enhancement of the migrating semidiurnal tide is a robust feature that has been reported for different SSWs (e.g., Jin et al., 2012; Maute et al., 2015; Siddiqui et al., 2021). Figure 12 presents examples of the migrating semidiurnal tide response to major SSWs over four boreal winters in UA-ICON(NWP). In each winter case, the top panel depicts the zonal-mean zonal wind at 60°N and 10 hPa ($\overline{U}$), along with the difference in temperature between the North Pole and the zonal average at 60°N at 10 hPa ($\overline{\Delta T}$). Reversal of the zonal-mean zonal wind, accompanied by a reversal of the meridional temperature gradient, signifies the occurrence of a major SSW. The bottom panel shows the amplitude of the migrating semidiurnal tide in temperature at 110 km derived using the method described in Yamazaki (2023). In all cases, the enhancement in the tidal amplitude is observed following the peak reversal of the zonal-mean zonal wind, consistent with earlier studies. The tidal response is similar during other boreal winters that contain major SSWs, which are not presented here. These results suggest that UA-ICON(NWP) may be well suited for studying the coupling between SSWs and variability in the middle and upper atmosphere.

7 Discussion, summary and conclusions

This work introduces a tuned version of the upper-atmosphere extension of the ICON model with the NWP physics package (UA-ICON(NWP)). It reasonably well represents the mean state and the variability of the MLT. Here, we document the parameter optimization for the Warner and McIntyre (1996) (WM96) gravity wave parameterization for the non-orographic and the Lott and Miller (1997) (LM97) parameterization for the orographic gravity waves in UA-ICON with the NWP physics package to achieve the presented results. To this aim, we apply UA-ICON(NWP) at a horizontal resolution of R2B4 ($\sim$160 km) and 120 layers up to an altitude of 150 km. By a series of perpetual January simulations, we demonstrate the effects of changing the tunable parameters of both, the orographic and non-orographic, gravity wave parameterizations. Based on these simulations, we chose one parameter setup to best perform for the middle and upper atmosphere concerning the climatology in the MLT and the variability during the northern hemisphere winter season. We recommend for the non-orographic WM96 parameterization to increase a dimensionless factor of the saturation momentum flux density spectrum and to decrease the total launch momentum flux and, in the LM97 parameterization, to adapt the low-level wake drag constant, the gravity wave drag constant, and the critical Froude number, as detailed in Table 3. With these settings, UA-ICON(NWP) has a sufficiently strong upper mesospheric eastward-directed zonal wind tendency (up to 140 m s^{-1} d^{-1}) to drive a mean meridional residual circulation strong enough to create the required adiabatic cooling of the summer mesopause region. The climatological seasonal averages of the polar summer mesopause temperatures of UA-ICON(NWP) are as low as shown by SABER in austral summer (< 150 K) and in boreal summer (< 140 K). However, the altitude and vertical extent of these low summer mesopause temperatures are slightly too low and too narrow in UA-ICON(NWP).

Introducing a stronger non-orographic gravity wave drag (NGWD) in UA-ICON(NWP) partly reverses the direction or decelerates the magnitude of the zonal mean zonal wind in the lower thermosphere from the prevailing eastward-directed flow in the stratosphere and mesosphere during the winter seasons to a westward-directed flow or a weak eastward-directed

flow in the MLT. The magnitude of these zonal wind changes in UA-ICON(NWP) agrees well with the URAP zonal mean zonal wind changes in these seasons. The vertical extent of the mesospheric polar vortex in UA-ICON(NWP), however, is limited to ~80 km, which is common behaviour of GCMs or CCMs with extension to the lower thermosphere, running at a coarse horizontal resolution and thereby relying on the parameterization of the NGWD, e.g. HAMMONIA (Schmidt et al., 2006), WACCM6 (Gettelman et al., 2019), or UA-ICON (version ua-icon-1.0) (Borchert et al., 2019). Increasing the horizontal resolution allows GCMs to resolve at least a fraction of the NGWD down to the mesoscale and at a sufficient horizontal resolution, they do not require GW parameterizations (e.g. Liu et al., 2014; Becker and Vadas, 2018, 2020; Stephan et al., 2020). The KMCM (Becker and Vadas, 2018) and HIAMCM (Becker and Vadas, 2020), both spectral models with a truncation of 240, 190 layers up to 1.5×10^{-5} hPa (KMCM) and 260 layers up to 6×10^{-9} hPa (HIAMCM) in the thermosphere, resolve horizontal wavelengths with $\lambda \sim 165$ km and do not parameterize any GWs. Becker and Vadas (2020) discuss the height of the MLT summer zonal wind reversal in HIAMCM, which simulates GWs explicitly, and compare it to CIRA86, stating the zonal wind reversal from westward to eastward flow is too high in altitude, which is a consequence of the eastward GW drag being too high by about 10 km. This contrasts with the coarser models, relying on GW parameterizations, where the wind reversal is too low in altitude. While both types of models, GW resolving and GW parameterizing, have problems modelling the summer MLT wind reversal correctly, Becker and Vadas (2020) state that on average, GW-resolving GCMs do not simulate the MLT eastward to westward reversal in winter, which is at least in better agreement with climatologies derived for local radar-observations. Smith (2012) discusses the discrepancies between zonal mean zonal wind climatologies derived from satellite data and localized radar observations and explains the deviations with planetary-scale variations which cause persistent longitudinal variations in the zonal wind. Hindley et al. (2022) show the difference of meteor radar-derived zonal wind over South Georgia (54° S, 30° W) and WACCM6. Both show the wind reversal from the westward to the eastward zonal wind in summer however, they differ in winter with the meteor radar showing an eastward zonal wind throughout the MLT as an extension of the polar vortex into the upper mesosphere, whereas WACCM6 shows the transition from eastward to westward zonal wind. UA-ICON(NWP) behaves similarly to WACCM6 which is typical for models with parameterized GWs. Using UA-ICON (version ua-icon-1.0 with ECHAM physics) in a high-resolution configuration (R2B7 $\sim$ 20 km horizontally, 180 layers) without any parameterized GW drag, Stephan et al. (2020) show that the model sufficiently generates resolved GW momentum flux in the MLT region to model realistic thermal and dynamic structures. Still, using wave-resolving UA-ICON versions remains a computational challenge for future model applications. So far, we recommend our tuned low-resolution version for an efficient simulation of the MLT region for long simulations or ensembles.

The mesospheric mean meridional residual circulation (MMC), driven by the dissipation of GWs, connects the summer MLT region with the respective lower mesospheric and stratospheric winter atmospheres, which results in a descending motion in the high latitudes and adiabatic warming of the stratopause regions. With increasing the parameterized GW-drag in UA-ICON(NWP) the MMC intensifies with the consequence that the winter mesopause temperatures rise, creating a warm bias compared to SABER observations. This is a drawback for the proper simulation of the summer MLT temperatures. It remains to investigate whether transient and horizontal GW propagation allowing non-orographic gravity wave parameterizations, (e.g Bölöni et al., 2021), could resolve the current numerical dilemma. Whereas our tuning attempt for the NGWD focused on

changing the saturation conditions for NGWs and the source strength, by varying parameters without latitudinal variation, Richter et al. (2010) tuned the NGWD in WACCM3 by introducing a source-oriented GW parametrization, accounting for variability in convective activity and frontal systems. One detail of their tuning success concerns the SH springtime transition of the zonal wind, which shifts to an earlier date. The transition to an easterly flow in 60 °S at 10-hPa occurs in early November for ERA-5 reanalysis data, which the UA-ICON(ECHAM) simulation matches perfectly. The UA-ICON(NWP) simulations show the transition in late November, which is only slightly shifted to a later date by the GWD tuning (Fig. 4, supplement), compared with the WACCM experiments shown in Fig. 10 of Richter et al. (2010) which appear at the end of December.

A relevant benchmark test for GCMs/CCMs extending to the mesosphere or lower thermosphere is their ability to model major SSWs with a realistic frequency and strength, including the related upward coupling to the mesosphere. Compared to the initial version of UA-ICON, mostly based on the ECHAM physics package (Borchert et al., 2019), the version presented in this work, based on the NWP physics package, has a significantly better representation of the stratospheric/mesospheric Northern Hemisphere winter polar vortex and its variability. Our statistical evaluation of SSWs includes a mesospheric coupling diagnostic (Zülicke et al., 2018), a geometric vortex diagnostic distinguishing split from displaced vortex SSW (Charlton and Polvani, 2007), and a wave preconditioning diagnostic (Bancalá et al., 2012). The overall frequency of 5.2 SSWs per decade is well in the range of 4.8–5.8 SSWs per decade, estimated from the reanalysis products. However, their intensity as quantified with the accumulated easterlies (I_{acc}) was found to be -31 m s^{-1}, less than the range of the observed -58– -90 m s^{-1}. Mesospheric and stratospheric temperatures are usually anti-correlated and this structure is simulated well with UA-ICON(NWP). Although the SSW events with a strong mesospheric response are slightly too frequent, the close coupling of the mesosphere with the stratosphere is well included. Hence, in a statistical sense, the model's performance in the stratosphere is essential for the model's performance in the mesosphere.

The tidal analyses showed the amplitude of the migrating diurnal and semidiurnal tides in temperature to be well represented in UA-ICON(NWP), with the latitudinal structure and the seasonal variability in an acceptable state, compared to SABER-derived tides. The enhancement of the migrating semidiurnal tide during major SSWs is well reproduced in UA-ICON(NWP), indicating a good representation of vertical coupling mechanisms in the model.

In conclusion, the UA-ICON (version ua-icon-2.1) at a horizontal resolution of ∼160 km is a highly performing upper atmosphere model available for vertical atmosphere coupling studies and investigating the MLT region. Besides, this paper has pointed out several challenges which need to be tackled in atmosphere modelling with UA-ICON. These are the lack of ability to tune equally well stratosphere and mesosphere, the equatorward bias of jet positions, the possibly related biases of the polar vortex in SSW strengths and wave-2 preconditioning, the too narrow and low cold summer MLT, or the winter polar vortex not extending high enough. We expect to solve these problems with high-resolution modelling to increase the fraction of the resolved GW drag, a method UA-ICON is particularly designed for.

Code availability. The model source code of ua-icon-2.1 used for the UA-ICON(NWP) simulations is published on Zenodo (Kunze et al., 2024), https://doi.org/10.5281/zenodo.13927890. It is based on the ICON open source release (ICON partnership (DWD, MPI-M, DKRZ,

KIT, and C2SM), 2024), ICON release 2024.01. World Data Center for Climate (WDCC) at DKRZ. https://doi.org/10.35089/WDCC/IconRelease01,
which is available under a BSD 3-clause license (see https://www.icon-model.org, last access Oct 2024).

Data availability. The data to reproduce the Figures is published on Zenodo (Kunze et al., 2025), https://doi.org/10.5281/zenodo.15030995.
ERA-5 reanalyses on pressure levels are available from the Copernicus Climate Data Store (Hersbach et al., 2023, https://doi.org/10.24381/cds.bd0915c6).
MERRA2 reanalyses are available from the Global Modeling and Assimilation Office (GMAO) (2015), MERRA-2 inst3_3d_asm_Np: 3d,3-
Hourly,Instantaneous,Pressure-Level,Assimilation,Assimilated Meteorological Fields V5.12.4, Greenbelt, MD, USA, Goddard Earth Sci-
ences Data and Information Services Center (GES DISC), Accessed: 2023-07-25, https://doi.org/10.5067/QBZ6MG944HW0. NCEP/NCAR
reanalyses are available at the URL https://downloads.psl.noaa.gov/Datasets/ncep.reanalysis/Dailies/pressure. SABER v2.0 data are avail-
able at the URL https://data.gats-inc.com/saber/custom/Temp_O3_H2O/v2.0/. Aura-MLS data are available at the URL https://data.gesdisc.
earthdata.nasa.gov/data.

Author contributions. MK adapted the UA-ICON parameterisations to achieve UA-ICON (ua-icon-version-2.1), ran the model computations,
and wrote large parts of the manuscript. CZ ran the stratosphere-mesosphere coupling diagnosis. TS and YY conducted the tidal analysis.
MK, CZ, TS, CCS, YY, CS designed the study and discussed and interpreted the results. SB and HS advised in model development and
discussed results. All authors contributed to and agreed with the manuscript.

Competing interests. The contact author has declared that neither of the authors has any competing interests.

Acknowledgements. This work used resources of the German Climate Computing Center (Deutsches Klimarechenzentrum, DKRZ) granted
by its Scientific Steering Committee (WLA) under project ID 1233.

References

Alexander, M. J. and Dunkerton, T. J.: A Spectral Parameterization of Mean-Flow Forcing due to Breaking Gravity Waves, J. Atmos. Sci., 56, 4167–4182, https://doi.org/10.1175/1520-0469(1999)056<4167:ASPOMF>2.0.CO;2, 1999.

Andrews, D. G. and McIntyre, M. E.: Planetary Waves in Horizontal and Vertical Shear: The Generalized Eliassen-Palm Relation and the Mean Zonal Acceleration, J. Atmos. Sci., 33, 2031–2048, https://doi.org/10.1175/1520-0469(1976)033<2031:PWIHAV>2.0.CO;2, 1976.

Andrews, D. G., Holton, J. R., and Leovy, C. B.: Basic Dynamics, in: International Geophysics, vol. 40, pp. 113–149, Academic Press, https://doi.org/10.1016/B978-0-12-058575-5.50008-6, 1987.

Baldwin, M. P., Ayarzagüena, B., Birner, T., Butchart, N., Butler, A. H., Charlton-Perez, A. J., Domeisen, D. I. V., Garfinkel, C. I., Garny, H., Gerber, E. P., Hegglin, M. I., Langematz, U., and Pedatella, N. M.: Sudden Stratospheric Warmings, Rev. Geophys., 59, 49, https://doi.org/10.1029/2020RG000708, 2021.

Bancalá, S., Krüger, K., and Giorgetta, M.: The preconditioning of major sudden stratospheric warmings, J. Geophys. Res.: Atmos., 117, n/a–n/a, https://doi.org/10.1029/2011JD016769, 2012.

Beagley, S. R., McLandress, C., Fomichev, V. I., and Ward, W. E.: The Extended Canadian Middle Atmosphere Model, Geophysical Research Letters, 27, 2529–2532, https://doi.org/https://doi.org/10.1029/1999GL011233, 2000.

Bechtold, P., Köhler, M., Jung, T., Doblas-Reyes, F., Leutbecher, M., Rodwell, M. J., Vitart, F., and Balsamo, G.: Advances in simulating atmospheric variability with the ECMWF model: From synoptic to decadal time-scales, Q.J.R. Meteorol. Soc., 134, 1337–1351, https://doi.org/10.1002/qj.289, 2008.

Becker, E.: Sensitivity of the upper mesosphere to the Lorenz energy cycle of the troposphere, J. Atmos. Sci., 66, 647–666, https://doi.org/10.1175/2008JAS2735.1, 2009.

Becker, E.: Dynamical Control of the Middle Atmosphere, Space Sci. Rev., 168, https://doi.org/10.1007/s11214-011-9841-5, 2012.

Becker, E. and Vadas, S. L.: Secondary Gravity Waves in the Winter Mesosphere: Results From a High-Resolution Global Circulation Model, J. Geophys. Res.: Atmos., pp. 1–15, https://doi.org/10.1002/2017JD027460, 2018.

Becker, E. and Vadas, S. L.: Explicit Global Simulation of Gravity Waves in the Thermosphere, J. Geophys. Res.: Space Physics, 125, https://doi.org/10.1029/2020JA028034, 2020.

Berger, U. and von Zahn, U.: Icy particles in the summer mesopause region: Three-dimensional modeling of their environment and two-dimensional modeling of their transport, J. Geophys. Res., 107, 1366, https://doi.org/10.1029/2001JA000316, 2002.

Bölöni, G., Kim, Y. H., Borchert, S., and Achatz, U.: Toward transient subgrid-scale gravity wave representation in atmospheric models. Part I: Propagation model including nondissipative wave mean-flow interactions, J. Atmos. Sci., 78, 1317–1338, https://doi.org/10.1175/JAS-D-20-0065.1, 2021.

Borchert, S., Zhou, G., Baldauf, M., Schmidt, H., Zängl, G., and Reinert, D.: The upper-atmosphere extension of the ICON general circulation model (version: Ua-icon-1.0), Geosci. Model Dev., 12, https://doi.org/10.5194/gmd-12-3541-2019, 2019.

Burrage, M. D., Wu, D. L., Skinner, W. R., Ortland, D. A., and Hays, P. B.: Latitude and seasonal dependence of the semidiurnal tide observed by the high-resolution Doppler imager, J. Geophys. Res., 100, 313–321, https://doi.org/10.1029/95jd00696, 1995.

Butchart, N.: The stratosphere: a review of the dynamics and variability, Weather Clim. Dynam., 3, 1237–1272, https://doi.org/10.5194/wcd-3-1237-2022, 2022.

Butler, A. H., Seidel, D. J., Hardiman, S. C., Butchart, N., Birner, T., and Match, A.: Defining Sudden Stratospheric Warmings, Bull. Amer. Meteor. Soc., 96, 1913–1928, https://doi.org/10.1175/BAMS-D-13-00173.1, 2015.

Butler, A. H., Sjoberg, J. P., Seidel, D. J., and Rosenlof, K. H.: A sudden stratospheric warming compendium, Earth Syst. Sci. Data, 9, 63–76, https://doi.org/10.5194/essd-9-63-2017, 2017.

655 Chapman, S. and Lindzen, R. S.: Atmospheric Tides, Springer Netherlands, Dordrecht, https://doi.org/10.1007/978-94-010-3399-2, 1969.

Charlton, A. J. and Polvani, L. M.: A new look at stratospheric sudden warmings. Part I: Climatology and modeling benchmarks, J. Clim., 20, 449–469, https://doi.org/10.1175/JCLI3996.1, 2007.

Charney, J. G. and Drazin, P. G.: Propagation of planetary-scale disturbances from the lower into the upper atmosphere, J. Geophys. Res., 66, 83–109, https://doi.org/10.1029/JZ066i001p00083, 1961.

660 Charuvil Asokan, H., Chau, J. L., Larsen, M. F., Conte, J. F., Marino, R., Vierinen, J., Baumgarten, G., and Borchert, S.: Validation of Multistatic Meteor Radar Analysis Using Modeled Mesospheric Dynamics: An Assessment of the Reliability of Gradients and Vertical Velocities, J. Geophys. Res.: Atmos., 127, https://doi.org/10.1029/2021JD036039, 2022.

Cohen, J., Barlow, M., Kushner, P. J., and Saito, K.: Stratosphere-troposphere coupling and links with Eurasian land surface variability, J. Clim., 20, 5335–5343, https://doi.org/10.1175/2007JCLI1725.1, 2007.

665 Dawkins, E. C., Feofilov, A., Rezac, L., Kutepov, A. A., Janches, D., Höffner, J., Chu, X., Lu, X., Mlynczak, M. G., and Russell, J.: Validation of SABER v2.0 Operational Temperature Data With Ground-Based Lidars in the Mesosphere-Lower Thermosphere Region (75–105 km), J. Geophys. Res.: Atmos., 123, 9916–9934, https://doi.org/10.1029/2018JD028742, 2018.

de la Cámara, A., Birner, T., and Albers, J. R.: Are Sudden Stratospheric Warmings Preceded by Anomalous Tropospheric Wave Activity?, J. Clim., 32, 7173–7189, https://doi.org/10.1175/JCLI-D-19-0269.1, 2019.

670 Domeisen, D. I., Garfinkel, C. I., and Butler, A. H.: The Teleconnection of El Niño Southern Oscillation to the Stratosphere, Rev. Geophys., 57, 5–47, https://doi.org/10.1029/2018RG000596, 2019.

Doms, G., Förstner, J., Heise, E., Herzog, H.-J., Mironov, D., Raschendorfer, M., Reinhardt, T., Ritter, B., Schrodin, R., Schulz, J.-P., and Vogel, G.: Consortium for Small-Scale Modelling A Description of the Nonhydrostatic Regional COSMO Model Part II : Physical Parameterization, www.Cosmo-Model.Org, p. 152, 2011.

675 Fomichev, V. I. and Blanchet, J. P.: Development of the new ccc/gcm longwave radiation model for extension into the middle atmosphere, Atmos. - Ocean, 33, 513–529, https://doi.org/10.1080/07055900.1995.9649543, 1995.

Fomichev, V. I., Blanchet, J. P., and Turner, D. S.: Matrix parameterization of the 15 μm CO2 band cooling in the middle and upper atmosphere for variable CO2 concentration, J. Geophys. Res.: Atmos., 103, 11 505–11 528, https://doi.org/10.1029/98JD00799, 1998.

Fomichev, V. I., Ward, W. E., Beagley, S. R., McLandress, C., McConnell, J. C., McFarlane, N. A., and Shepherd, T. G.: Ex-
680 tended Canadian Middle Atmosphere Model: Zonal-mean climatology and physical parameterizations, J. Geophys. Res.: Atmos., 107, https://doi.org/10.1029/2001JD000479, 2002.

Forbes, J. M.: Tidal and Planetary Waves, in: Geophys. Monogr. Ser., vol. 87, pp. 67–87, American Geophysical Union, https://doi.org/10.1029/GM087p0067, 1995.

Forbes, J. M. and Garrett, H. B.: Theoretical studies of atmospheric tides, Rev. Geophys., 17, 1951–1981,
685 https://doi.org/10.1029/RG017i008p01951, 1979.

Forbes, J. M., Zhang, X., Palo, S., Russell, J., Mertens, C. J., and Mlynczak, M.: Tidal variability in the ionospheric dynamo region, J. Geophys. Res.: Space Physics, 113, 1–17, https://doi.org/10.1029/2007JA012737, 2008.

Gan, Q., Du, J., Ward, W. E., Beagley, S. R., Fomichev, V. I., and Zhang, S.: Climatology of the diurnal tides from eCMAM30 (1979 to 2010) and its comparison with SABER, Earth, Planets and Space, 66, 103, https://doi.org/10.1186/1880-5981-66-103, 2014.

690 García-Rodríguez, M., Añel, J. A., and Rodeiro-Iglesias, J.: Assessing and improving the quality of Fortran code in scientific software: FortranAnalyser, Software Impacts, 21, 100 692, https://doi.org/10.1016/j.simpa.2024.100692, 2024.

Gelaro, R., McCarty, W., Suárez, M. J., Todling, R., Molod, A., Takacs, L., Randles, C. A., Darmenov, A., Bosilovich, M. G., Reichle, R., Wargan, K., Coy, L., Cullather, R., Draper, C., Akella, S., Buchard, V., Conaty, A., da Silva, A. M., Gu, W., Kim, G.-K., Koster, R., Lucchesi, R., Merkova, D., Nielsen, J. E., Partyka, G., Pawson, S., Putman, W., Rienecker, M., Schubert, S. D., Sienkiewicz, M.,
695 and Zhao, B.: The Modern-Era Retrospective Analysis for Research and Applications, Version 2 (MERRA-2), J. Clim., 30, 5419–5454, https://doi.org/10.1175/JCLI-D-16-0758.1, 2017.

Gettelman, A., Mills, M. J., Kinnison, D. E., Garcia, R. R., Smith, A. K., Marsh, D. R., Tilmes, S., Vitt, F., Bardeen, C. G., McInerney, J., Liu, H., Solomon, S. C., Polvani, L. M., Emmons, L. K., Lamarque, J., Richter, J. H., Glanville, A. S., Bacmeister, J. T., Phillips, A. S., Neale, R. B., Simpson, I. R., DuVivier, A. K., Hodzic, A., and Randel, W. J.: The Whole Atmosphere Community Climate Model Version
700 6 (WACCM6), J. Geophys. Res.: Atmos., 6, 380–403, https://doi.org/10.1029/2019jd030943, 2019.

Gill, A. E.: Atmosphere—Ocean Dynamics, vol. 30 of *International Geophysics*, Elsevier, https://doi.org/10.1016/S0074-6142(08)X6002-4, 1982.

Giorgetta, M. A., Brokopf, R., Crueger, T., Esch, M., Fiedler, S., Helmert, J., Hohenegger, C., Kornblueh, L., Köhler, M., Manzini, E., Mauritsen, T., Nam, C., Raddatz, T., Rast, S., Reinert, D., Sakradzija, M., Schmidt, H., Schneck, R., Schnur, R., Silvers, L., Wan, H.,
705 Zängl, G., and Stevens, B.: ICON-A, the atmosphere component of the ICON Earth System Model. Part I: Model Description, J. Adv. Model. Earth Syst., 10, 1613–1637, https://doi.org/10.1029/2017MS001242, 2018.

Giorgetta, M. A., Sawyer, W., Lapillonne, X., Adamidis, P., Alexeev, D., Clément, V., Dietlicher, R., Engels, J. F., Esch, M., Franke, H., Frauen, C., Hannah, W. M., Hillman, B. R., Kornblueh, L., Marti, P., Norman, M. R., Pincus, R., Rast, S., Reinert, D., Schnur, R., Schulzweida, U., and Stevens, B.: The ICON-A model for direct QBO simulations on GPUs (version icon-cscs:baf28a514), Geosci. Model
710 Dev., 15, 6985–7016, https://doi.org/10.5194/gmd-15-6985-2022, 2022.

Hagan, M. E. and Forbes, J. M.: Migrating and nonmigrating diurnal tides in the middle and upper atmosphere excited by tropospheric latent heat release, J. Geophys. Res.: Atmos., 107, ACL 6–1–ACL 6–15, https://doi.org/10.1029/2001JD001236, 2002.

Hagan, M. E. and Forbes, J. M.: Migrating and nonmigrating semidiurnal tides in the upper atmosphere excited by tropospheric latent heat release, J. Geophys. Res.: Space Physics, 108, 1–14, https://doi.org/10.1029/2002JA009466, 2003.

715 Hall, R. J., Mitchell, D. M., Seviour, W. J. M., and Wright, C. J.: Persistent Model Biases in the CMIP6 Representation of Stratospheric Polar Vortex Variability, J. Geophys. Res.: Atmos., 126, https://doi.org/10.1029/2021JD034759, 2021.

Hardiman, S. C., Andrews, D. G., White, A. a., Butchart, N., and Edmond, I.: Using Different Formulations of the Transformed Eulerian Mean Equations and Eliassen–Palm Diagnostics in General Circulation Models, J. Atmos. Sci., 67, 1983–1995, https://doi.org/10.1175/2010JAS3355.1, 2010.

720 Harvey, V. L., Randall, C. E., Becker, E., Smith, A. K., Bardeen, C. G., France, J. A., and Goncharenko, L. P.: Evaluation of the Mesospheric Polar Vortices in WACCM, J. Geophys. Res.: Atmos., 124, 10 626–10 645, https://doi.org/10.1029/2019JD030727, 2019.

Hersbach, H., Bell, B., Berrisford, P., Hirahara, S., Horányi, A., Muñoz-Sabater, J., Nicolas, J., Peubey, C., Radu, R., Schepers, D., Simmons, A., Soci, C., Abdalla, S., Abellan, X., Balsamo, G., Bechtold, P., Biavati, G., Bidlot, J., Bonavita, M., Chiara, G., Dahlgren, P., Dee, D., Diamantakis, M., Dragani, R., Flemming, J., Forbes, R., Fuentes, M., Geer, A., Haimberger, L., Healy, S., Hogan, R. J., Hólm, E.,
725 Janisková, M., Keeley, S., Laloyaux, P., Lopez, P., Lupu, C., Radnoti, G., Rosnay, P., Rozum, I., Vamborg, F., Villaume, S., and Thépaut, J.: The ERA5 global reanalysis, Q.J.R. Meteorol. Soc., 146, 1999–2049, https://doi.org/10.1002/qj.3803, 2020.

Hersbach, H., Bell, B., Berrisford, P., Biavati, G., Horányi, A., Muñoz-Sabater, J., Nicolas, J., Peubey, C., Radu, R., Rozum, I., Schepers, D., Soci, C., Dee, D., and Thépaut, J.: ERA5 monthly averaged data on pressure levels from 1940 to present. Copernicus Climate Change Service (C3S) Climate Data Store (CDS), https://doi.org/10.24381/cds.6860a573, 2023.

730 Hindley, N. P., Mitchell, N. J., Cobbett, N., Smith, A. K., Fritts, D. C., Janches, D., Wright, C. J., and Moffat-Griffin, T.: Radar observations of winds, waves and tides in the mesosphere and lower thermosphere over South Georgia island (54° S, 36° W) and comparison with WACCM simulations, Atmos. Chem. Phys., 22, 9435–9459, https://doi.org/10.5194/acp-22-9435-2022, 2022.

Hines, C. O.: Doppler-spread parameterization of gravity-wave momentum deposition in the middle atmosphere. Part 1: Basic formulation, J. Atmosph. Solar-Terr. Phys., 59, 371–386, https://doi.org/10.1016/S1364-6826(96)00079-X, 1997a.

735 Hines, C. O.: Doppler-spread parameterization of gravity-wave momentum deposition in the middle atmosphere. Part 2: Broad and quasi monochromatic spectra, and implementation, J. Atmosph. Solar-Terr. Phys., 59, 387–400, https://doi.org/10.1016/S1364-6826(96)00080-6, 1997b.

Hogan, R. J. and Bozzo, A.: ECRAD: A new radiation scheme for the IFS, ECMWF Tech., 787, 1–33, 2016.

Holton, J. R. and Tan, H.-C.: The Influence of the Equatorial Quasi-Biennial Oscillation on the Global Circulation at 50 mb, J. Atmos. Sci.,
740 37, 2200–2208, https://doi.org/10.1175/1520-0469(1980)037<2200:TIOTEQ>2.0.CO;2, 1980.

Hong, S.-S. and Lindzen, R. S.: Solar Semidiurnal Tide in the Thermosphere, J. Atmos. Sci., 33, 135–153, https://doi.org/10.1175/1520-0469(1976)033<0135:SSTITT>2.0.CO;2, 1976.

Huang, T., Walters, S., and Brasseur, G. P.: Description of SOCRATES- A Chemical Dynamical Radiative Two-Dimensional Model, Tech. Rep. March, University Corporation for Atmospheric Research, https://doi.org/10.5065/D6K0726C, 1998.

745 ICON partnership (DWD, MPI-M, DKRZ, KIT, and C2SM): ICON release 2024.01, https://doi.org/10.35089/WDCC/IconRelease01, 2024.

Jin, H., Miyoshi, Y., Pancheva, D., Mukhtarov, P., Fujiwara, H., and Shinagawa, H.: Response of migrating tides to the stratospheric sudden warming in 2009 and their effects on the ionosphere studied by a whole atmosphere-ionosphere model GAIA with COSMIC and TIMED/SABER observations, J. Geophys. Res.: Space Physics, 117, https://doi.org/10.1029/2012JA017650, 2012.

Jones, M., Forbes, J. M., and Hagan, M. E.: Tidal-induced net transport effects on the oxygen distribution in the thermosphere, Geophys.
750 Res. Lett., 41, 5272–5279, https://doi.org/10.1002/2014GL060698, 2014.

Jungclaus, J. H., Lorenz, S. J., Schmidt, H., Brovkin, V., Brüggemann, N., Chegini, F., Crüger, T., De-Vrese, P., Gayler, V., Giorgetta, M. A., Gutjahr, O., Haak, H., Hagemann, S., Hanke, M., Ilyina, T., Korn, P., Kröger, J., Linardakis, L., Mehlmann, C., Mikolajewicz, U., Müller, W. A., Nabel, J. E. M. S., Notz, D., Pohlmann, H., Putrasahan, D. A., Raddatz, T., Ramme, L., Redler, R., Reick, C. H., Riddick, T., Sam, T., Schneck, R., Schnur, R., Schupfner, M., Storch, J., Wachsmann, F., Wieners, K., Ziemen, F., Stevens, B., Marotzke, J., and Claussen,
755 M.: The ICON Earth System Model Version 1.0, J. Adv. Model. Earth Syst., 14, https://doi.org/10.1029/2021MS002813, 2022.

Kalnay, E., Kanamitsu, M., Kistler, R., Collins, W., Deaven, D., Gandin, L., Iredell, M., Saha, S., White, G., Woollen, J., Zhu, Y., Leetmaa, A., Reynolds, R., Chelliah, M., Ebisuzaki, W., Higgins, W., Janowiak, J., Mo, K. C., Ropelewski, C., Wang, J., Jenne, R., and Joseph, D.: The NCEP/NCAR 40-Year Reanalysis Project, Bull. Amer. Meteor. Soc., 77, 437–471, https://doi.org/10.1175/1520-0477(1996)077<0437:TNYRP>2.0.CO;2, 1996.

760 Karami, K., Mehrdad, S., and Jacobi, C.: Response of the resolved planetary wave activity and amplitude to turned off gravity waves in the UA-ICON general circulation model, J. Atmos. Solar-Terrestrial Phys., 241, 105 967, https://doi.org/10.1016/j.jastp.2022.105967, 2022.

Karami, K., Borchert, S., Eichinger, R., Jacobi, C., Kuchar, A., Mehrdad, S., Pisoft, P., and Sacha, P.: The Climatology of Elevated Stratopause Events in the UA-ICON Model and the Contribution of Gravity Waves, J. Geophys. Res.: Atmos., 128, https://doi.org/10.1029/2022JD037907, 2023.

765 Kim, Y. H. and Achatz, U.: Interaction Between Stratospheric Kelvin Waves and Gravity Waves in the Easterly QBO Phase, Geophys. Res. Lett., 48, 1–8, https://doi.org/10.1029/2021GL095226, 2021.

Kim, Y.-H. H., Bölöni, G., Borchert, S., Chun, H.-Y. Y., and Achatz, U.: Toward Transient Subgrid-Scale Gravity Wave Representation in Atmospheric Models. Part II: Wave Intermittency Simulated with Convective Sources, J. Atmos. Sci., 78, 1339–1357, https://doi.org/10.1175/JAS-D-20-0066.1, 2021.

770 Kinne, S., O'Donnel, D., Stier, P., Kloster, S., Zhang, K., Schmidt, H., Rast, S., Giorgetta, M., Eck, T. F., and Stevens, B.: MAC-v1: A new global aerosol climatology for climate studies, J. Adv. Model. Earth Syst., 5, 704–740, https://doi.org/10.1002/jame.20035, 2013.

Kistler, R., Collins, W., Saha, S., White, G., Woollen, J., Kalnay, E., Chelliah, M., Ebisuzaki, W., Kanamitsu, M., Kousky, V., van den Dool, H., Jenne, R., and Fiorino, M.: The NCEP–NCAR 50–Year Reanalysis: Monthly Means CD–ROM and Documentation, Bull. Amer. Meteor. Soc., 82, 247–267, https://doi.org/10.1175/1520-0477(2001)082<0247:TNNYRM>2.3.CO;2, 2001.

775 Kockarts, G.: Nitric oxide cooling in the terrestrial thermosphere, Geophys. Res. Lett., 7, 137–140, https://doi.org/10.1029/GL007i002p00137, 1980.

Kunze, M., Zülicke, C., Siddiqui, T. A., Stephan, C. C., Yamazaki, Y., Stolle, C., Borchert, S., and Schmidt, H.: Supplementary information on - UA-ICON with NWP physics package (version: ua-icon-2.1): mean state and variability of the middle atmosphere, https://doi.org/10.5281/zenodo.13927891, 2024.

780 Kunze, M., Zülicke, C., Siddiqui, T. A., Stephan, C. C., Yamazaki, Y., Stolle, C., Borchert, S., and Schmidt, H.: Supplementary data for Figures of "UA-ICON with NWP physics package (version: ua-icon-2.1): mean state and variability of the middle atmosphere", https://doi.org/10.5281/zenodo.15030995, 2025.

Labitzke, K.: Stratospheric-mesospheric midwinter disturbances: A summary of observed characteristics, J. Geophys. Res., 86, 9665, https://doi.org/10.1029/JC086iC10p09665, 1981.

785 Labitzke, K.: Sunspots, the QBO, and the stratospheric temperature in the north polar region, Geophys. Res. Lett., 14, 535–537, https://doi.org/10.1029/GL014i005p00535, 1987.

Limpasuvan, V., Orsolini, Y. J., Chandran, A., Garcia, R. R., and Smith, A. K.: On the composite response of the MLT to major sudden stratospheric warming events with elevated stratopause, J. Geophys. Res.: Atmos., 121, 4518–4537, https://doi.org/10.1002/2015JD024401, 2016.

790 Liu, H.-L., McInerney, J. M., Santos, S., Lauritzen, P. H., Taylor, M. A., and Pedatella, N. M.: Gravity waves simulated by high-resolution Whole Atmosphere Community Climate Model, Geophys. Res. Lett., 41, 9106–9112, https://doi.org/10.1002/2014GL062468, 2014.

Liu, H. L., Bardeen, C. G., Foster, B. T., Lauritzen, P., Liu, J., Lu, G., Marsh, D. R., Maute, A., McInerney, J. M., Pedatella, N. M., Qian, L., Richmond, A. D., Roble, R. G., Solomon, S. C., Vitt, F. M., and Wang, W.: Development and Validation of the Whole Atmosphere Community Climate Model With Thermosphere and Ionosphere Extension (WACCM-X 2.0), J. Adv. Model. Earth Syst., 10, 381–402,
795 https://doi.org/10.1002/2017MS001232, 2018a.

Liu, J., Liu, H., Wang, W., Burns, A. G., Wu, Q., Gan, Q., Solomon, S. C., Marsh, D. R., Qian, L., Lu, G., Pedatella, N. M., McInerney, J. M., Russell III, J. M., and Schreiner, W. S.: First Results From the Ionospheric Extension of WACCM-X During the Deep Solar Minimum Year of 2008, Journal of Geophysical Research: Space Physics, 123, 1534–1553, https://doi.org/https://doi.org/10.1002/2017JA025010, 2018b.

800 Livesey, N. J., Read, W. G., Wagner, P. A., Froidevaux, L., Santee, M. L., Schwartz, M. J., Lambert, A., Valle, L. F. M., Pumphrey, H. C., Manney, G. L., Fuller, R. A., Jarnot, R. F., Knosp, B. W., and Lay, R. R.: Aura Microwave Limb Sounder (MLS) Version 5.0x Level 2 and 3 data quality and description document, https://doi.org/10.5067/Aura/MLS/DATA2520, 2022.

Lohmann, U. and Roeckner, E.: Design and performance of a new cloud microphysics scheme developed for the ECHAM general circulation model, Clim. Dyn., 12, 557–572, https://doi.org/10.1007/BF00207939, 1996.

805 Lott, F.: Alleviation of Stationary Biases in a GCM through a Mountain Drag Parameterization Scheme and a Simple Representation of Mountain Lift Forces, Mon. Weather Rev., 127, 788–801, https://doi.org/10.1175/1520-0493(1999)127<0788:AOSBIA>2.0.CO;2, 1999.

Lott, F. and Miller, M. J.: A new subgrid-scale orographic drag parametrization: Its formulation and testing, Q.J.R. Meteorol. Soc., 123, 101–127, https://doi.org/10.1002/qj.49712353704, 1997.

Manzini, E., Giorgetta, M. A., Esch, M., Kornblueh, L., and Roeckner, E.: The influence of sea surface temperatures on the northern winter
810 stratosphere: Ensemble simulations with the MAECHAM5 model, J. Clim., 19, 3863–3881, https://doi.org/10.1175/JCLI3826.1, 2006.

Matthes, K., Funke, B., Andersson, M. E., Barnard, L., Beer, J., Charbonneau, P., Clilverd, M. A., Dudok de Wit, T., Haberreiter, M., Hendry, A., Jackman, C. H., Kretzschmar, M., Kruschke, T., Kunze, M., Langematz, U., Marsh, D. R., Maycock, A. C., Misios, S., Rodger, C. J., Scaife, A. A., Seppälä, A., Shangguan, M., Sinnhuber, M., Tourpali, K., Usoskin, I., van de Kamp, M., Verronen, P. T., and Versick, S.: Solar forcing for CMIP6 (v3.2), Geosci. Model Dev., 10, 2247–2302, https://doi.org/10.5194/gmd-10-2247-2017, 2017.

815 Maute, A., Hagan, M., Yudin, V., Liu, H.-L., and Yizengaw, E.: Causes of the longitudinal differences in the equatorial vertical E× B drift during the 2013 SSW period as simulated by the TIME-GCM, Journal of Geophysical Research: Space Physics, 120, 5117–5136, https://doi.org/doi.org/10.1002/2015JA021126, 2015.

Mcinturff, R. M.: Stratospheric warmings: Synoptic, dynamic and general-circulation aspects, Natl. Aeronaut. Sp. Adm. Sci. Tech. Inf. Off., http://hdl.handle.net/2060/19780010687, 1978.

820 McLandress, C.: The Seasonal Variation of the Propagating Diurnal Tide in the Mesosphere and Lower Thermosphere. Part I: The Role of Gravity Waves and Planetary Waves, J. Atmos. Sci., 59, 907–922, https://doi.org/10.1175/1520-0469(2002)059<0907:TSVOTP>2.0.CO;2, 2002a.

McLandress, C.: The Seasonal Variation of the Propagating Diurnal Tide in the Mesosphere and Lower Thermosphere. Part II: The Role of Tidal Heating and Zonal Mean Winds, J. Atmos. Sci., 59, 907–922, https://doi.org/10.1175/1520-
825 0469(2002)059<0907:TSVOTP>2.0.CO;2, 2002b.

McLandress, C. and Scinocca, J. F.: The GCM Response to Current Parameterizations of Nonorographic Gravity Wave Drag, J. Atmos. Sci., 62, 2394–2413, https://doi.org/10.1175/JAS3483.1, 2005.

McLandress, C., Shepherd, G. G., and Solheim, B. H.: Satellite observations of thermospheric tides: Results from the Wind Imaging Inter-ferometer on UARS, J. Geophys. Res.: Atmos., 101, 4093–4114, https://doi.org/10.1029/95JD03359, 1996.

830 Mlawer, E. J., Taubman, S. J., Brown, P. D., Iacono, M. J., and Clough, S. A.: Radiative transfer for inhomogeneous atmospheres: RRTM, a validated correlated-k model for the longwave, J. Geophys. Res.: Atmos., 102, 16 663–16 682, https://doi.org/10.1029/97JD00237, 1997.

Newman, P. A. and Rosenfield, J. E.: Stratospheric thermal damping times, Geophys. Res. Lett., 24, 433–436, https://doi.org/10.1029/96GL03720, 1997.

Nordeng, T. E.: Extended versions of the convection parametrization scheme at {ECMWF} and their impact on the mean and transient
835 activity of the model in the tropics, Tech. Rep. 206, Eur. Cent for Medium-Range Weather Forecasts, Reading, U. K, 1994.

Oberheide, J., Forbes, J. M., Zhang, X., and Bruinsma, S. L.: Climatology of upward propagating diurnal and semidiurnal tides in the thermosphere, J. Geophys. Res.: Space Physics, 116, n/a–n/a, https://doi.org/10.1029/2011JA016784, 2011.

Ogibalov, V. and Fomichev, V.: Parameterization of solar heating by the near IR CO2 bands in the mesosphere, Adv. Space Res., 32, 759–764, https://doi.org/10.1016/S0273-1177(03)80069-8, 2003.

840   Okui, H., Sato, K., Koshin, D., and Watanabe, S.: Formation of a Mesospheric Inversion Layer and the Subsequent Elevated Stratopause Associated With the Major Stratospheric Sudden Warming in 2018/19, J. Geophys. Res.: Atmos., 126, 1–22, https://doi.org/10.1029/2021JD034681, 2021.

Orr, A., Bechtold, P., Scinocca, J., Ern, M., and Janiskova, M.: Improved Middle Atmosphere Climate and Forecasts in the ECMWF Model through a Nonorographic Gravity Wave Drag Parameterization, J. Clim., 23, 5905–5926, https://doi.org/10.1175/2010JCLI3490.1, 2010.

845   Pedatella, N. M., Fuller-Rowell, T., Wang, H., Jin, H., Miyoshi, Y., Fujiwara, H., Shinagawa, H., Liu, H.-L., Sassi, F., Schmidt, H., Matthias, V., and Goncharenko, L.: The neutral dynamics during the 2009 sudden stratosphere warming simulated by different whole atmosphere models, Journal of Geophysical Research: Space Physics, 119, 1306–1324, https://doi.org/https://doi.org/10.1002/2013JA019421, 2014.

Pincus, R. and Stevens, B.: Paths to accuracy for radiation parameterizations in atmospheric models, J. Adv. Model. Earth Syst., 5, 225–233, https://doi.org/10.1002/jame.20027, 2013.

850   Pithan, F., Angevine, W., and Mauritsen, T.: Improving a global model from the boundary layer: Total turbulent energy and the neutral limit Prandtl number, J. Adv. Model. Earth Syst., 7, 791–805, https://doi.org/10.1002/2014MS000382, 2015.

Qian, L., Burns, A., and Yue, J.: Evidence of the Lower Thermospheric Winter-to-Summer Circulation From SABER CO_2 Observations, Geophys. Res. Lett., 44, 10,100–10,107, https://doi.org/10.1002/2017GL075643, 2017.

Raschendorfer, M.: The New Turbulence Parameterization of LM, Tech. rep., Deutscher Wetterdienst, http://www.cosmo-model.org/, 2001.

855   Richards, P. G., Fennelly, J. a., and Torr, D. G.: EUVAC: A solar EUV Flux Model for aeronomic calculations, J. Geophys. Res., 99, 8981, https://doi.org/10.1029/94JA00518, 1994.

Richter, J. H., Sassi, F., Garcia, R. R., , K., and Fischer, C. A.: Dynamics of the middle atmosphere as simulated by the Whole Atmosphere Community Climate Model, version 3 (WACCM3), J. Geophys. Res.: Atmos., 113, https://doi.org/10.1029/2007JD009269, 2008.

Richter, J. H., Sassi, F., and Garcia, R. R.: Toward a physically based gravity wave source parameterization in a general circulation model, J.
860   Atmos. Sci., 67, 136–156, https://doi.org/10.1175/2009JAS3112.1, 2010.

Russell III, J. M., Mlynczak, M. G., Gordley, L. L., Tansock, Jr., J. J., and Esplin, R. W.: Overview of the SABER experiment and preliminary calibration results, in: Opt. Spectrosc. Tech. Instrum. Atmos. Sp. Res. III, edited by Larar, A. M., vol. 3756, p. 277, https://doi.org/10.1117/12.366382, 1999.

Sassi, F., Kinnison, D., Boville, B. A., Garcia, R. R., and Roble, R.: Effect of El Niño–Southern Oscillation on the dynamical, thermal, and
865   chemical structure of the middle atmosphere, J. Geophys. Res.: Atmos., 109, https://doi.org/10.1029/2003JD004434, 2004.

Sato, K. and Nomoto, M.: Gravity Wave–Induced Anomalous Potential Vorticity Gradient Generating Planetary Waves in the Winter Mesosphere, J. Atmos. Sci., 72, 3609–3624, https://doi.org/10.1175/JAS-D-15-0046.1, 2015.

Scherhag, R.: Die explosionsartigen Stratosphärenerwärmungen des Spätwinters 1951/52, Ber. des DWD, 38, 51–62, 1952.

Schimanke, S., Körper, J., Spangehl, T., and Cubasch, U.: Multi-decadal variability of sudden stratospheric warmings in an AOGCM, Geo-
870   phys. Res. Lett., 38, n/a–n/a, https://doi.org/10.1029/2010GL045756, 2011.

Schmidt, H., Brasseur, G. P., Charron, M., Manzini, E., Giorgetta, M. a., Diehl, T., Fomichev, V. I., Kinnison, D., Marsh, D., and Walters, S.: The HAMMONIA Chemistry Climate Model: Sensitivity of the Mesopause Region to the 11-Year Solar Cycle and CO_2 Doubling, J. Clim., 19, 3903–3931, https://doi.org/10.1175/JCLI3829.1, 2006.

Seifert, A.: A Revised Cloud Microphysical Parameterization for COSMO-LME, COSMO Newsl., pp. 25–28, 2008.

875   Siddiqui, T. A., Yamazaki, Y., Stolle, C., Maute, A., Laštovička, J., Edemskiy, I., Mošna, Z., and Sivakandan, M.: Understanding the total electron content variability over Europe during 2009 and 2019 SSWs, JGRSP, 126, e2020JA028 751, https://doi.org/10.1029/2020JA028751, 2021.

Siddiqui, T. A., Chau, J. L., Stolle, C., and Yamazaki, Y.: Migrating solar diurnal tidal variability during northern and southern hemisphere sudden stratospheric warmings, Earth, Planets and Space, 74, 101, https://doi.org/10.1186/s40623-022-01661-y, 2022.

880 Smith, A. K.: Global Dynamics of the MLT, Surv. Geophys., 33, 1177–1230, https://doi.org/10.1007/s10712-012-9196-9, 2012.

Stephan, C. C., Schmidt, H., Zülicke, C., and Matthias, V.: Oblique Gravity Wave Propagation During Sudden Stratospheric Warmings, J. Geophys. Res.: Atmos., 125, 2019JD031 528, https://doi.org/10.1029/2019JD031528, 2020.

Stober, G., Kuchar, A., Pokhotelov, D., Liu, H., Liu, H.-L., Schmidt, H., Jacobi, C., Baumgarten, K., Brown, P., Janches, D., Murphy, D., Kozlovsky, A., Lester, M., Belova, E., Kero, J., and Mitchell, N.: Interhemispheric differences of mesosphere–lower thermosphere winds

885 and tides investigated from three whole-atmosphere models and meteor radar observations, Atmos. Chem. Phys., 21, 13 855–13 902, https://doi.org/10.5194/acp-21-13855-2021, 2021.

Strobel, D. F.: Parameterization of the atmospheric heating rate from 15 to 120 km due to O_2 and O_3 absorption of solar radiation, J. Geophys. Res., 83, 6225, https://doi.org/10.1029/JC083iC12p06225, 1978.

Sundqvist, H., Berge, E., and Kristjánsson, J. E.: Condensation and Cloud Parameterization Studies with a Mesoscale Numerical Weather

890 Prediction Model, Mon. Weather Rev., 117, 1641–1657, https://doi.org/10.1175/1520-0493(1989)117<1641:CACPSW>2.0.CO;2, 1989.

Swinbank, R. and Ortland, D. A.: Compilation of wind data for the Upper Atmosphere Research Satellite (UARS) Reference Atmosphere Project, J. Geophys. Res., 108, 4615, https://doi.org/10.1029/2002JD003135, 2003.

Taylor, K. E., Williamson, D. L., and Zwiers, F. W.: The Sea Surface Temperature and Sea-Ice Concentration Boundary Conditions for AMIP II Simulations, Program for Climate Model Diagnosis and Intercomparison (PCMDI) Report 60, Lawrence Livermore Natl. Lab.

895 Livermore, Calif., pp. 1–28, http://www-pcmdi.llnl.gov/publications/ab60.html, 2000.

Tiedtke, M.: A comprehensive mass flux scheme for cumulus parameterization in large-scale models, Mon. Weather Rev., 117, 1179–1800, https://doi.org/10.1175/1520-0493(1989)117<1779:ACMFSF>2.0.CO;2, 1989.

Vincent, R. A.: The dynamics of the mesosphere and lower thermosphere: a brief review, Prog. Earth Planet. Sci., 2, https://doi.org/10.1186/s40645-015-0035-8, 2015.

900 Wallis, S., Schmidt, H., and von Savigny, C.: Impact of a strong volcanic eruption on the summer middle atmosphere in UA-ICON simulations, Atmos. Chem. Phys., 23, 7001–7014, https://doi.org/10.5194/acp-23-7001-2023, 2023.

Wang, N., Qian, L., Yue, J., Wang, W., Mlynczak, M. G., and Russell, J. M.: Climatology of Mesosphere and Lower Thermosphere Residual Circulations and Mesopause Height Derived From SABER Observations, J. Geophys. Res.: Atmos., 127, 1–14, https://doi.org/10.1029/2021jd035666, 2022.

905 Warner, C. D. and McIntyre, M. E.: On the Propagation and Dissipation of Gravity Wave Spectra through a Realistic Middle Atmosphere, J. Atmos. Sci., 53, 3213–3235, https://doi.org/10.1175/1520-0469(1996)053<3213:OTPADO>2.0.CO;2, 1996.

Watanabe, S. and Miyahara, S.: Quantification of the gravity wave forcing of the migrating diurnal tide in a gravity wave–resolving general circulation model, J. Geophys. Res., 114, D07 110, https://doi.org/10.1029/2008JD011218, 2009.

Wu, Z. and Reichler, T.: Variations in the frequency of stratospheric sudden warmings in CMIP5 and CMIP6 and possible causes, J. Clim.,

910 33, 10 305–10 320, https://doi.org/10.1175/JCLI-D-20-0104.1, 2020.

Yamazaki, Y.: A method to derive Fourier–wavelet spectra for the characterization of global-scale waves in the mesosphere and lower thermosphere and its MATLAB and Python software (fourierwavelet v1. 1), Geoscientific Model Development, 16, 4749–4766, https://doi.org/10.5194/gmd-16-4749-2023, 2023.

Yamazaki, Y. and Richmond, A. D.: A theory of ionospheric response to upward-propagating tides: Electrodynamic effects and tidal mixing

915 effects, J. Geophys. Res.: Space Physics, 118, 5891–5905, https://doi.org/10.1002/jgra.50487, 2013.

Yamazaki, Y. and Siddiqui, T. A.: Symmetric and antisymmetric solar migrating semidiurnal tides in the mesosphere and lower thermosphere, J. Geophys. Res.: Atmos., 129, e2023JD040 222, https://doi.org/10.1029/2023JD040222, 2024.

Yamazaki, Y., Harding, B. J., Qiu, L., Stolle, C., Siddiqui, T. A., Miyoshi, Y., Englert, C. R., and England, S. L.: Monthly Climatologies of Zonal-Mean and Tidal Winds in the Thermosphere as Observed by ICON/MIGHTI During April 2020–March 2022, Earth Space Sci., 10, 1–30, https://doi.org/10.1029/2023EA002962, 2023.

Zhang, X., Forbes, J. M., and Hagan, M. E.: Longitudinal variation of tides in the MLT region: 1. Tides driven by tropospheric net radiative heating, J. Geophys. Res.: Space Physics, 115, 1–16, https://doi.org/10.1029/2009JA014897, 2010a.

Zhang, X., Forbes, J. M., and Hagan, M. E.: Longitudinal variation of tides in the MLT region: 2. Relative effects of solar radiative and latent heating, J. Geophys. Res.: Space Physics, 115, 1–19, https://doi.org/10.1029/2009JA014898, 2010b.

Zülicke, C. and Becker, E.: The structure of the mesosphere during sudden stratospheric warmings in a global circulation model, J. Geophys. Res.: Atmos., 118, 2255–2271, https://doi.org/10.1002/jgrd.50219, 2013.

Zülicke, C., Becker, E., Matthias, V., Peters, D. H. W., Schmidt, H., Liu, H.-L., Ramos, L. d. l. T., and Mitchell, D. M.: Coupling of Stratospheric Warmings with Mesospheric Coolings in Observations and Simulations, J. Clim., 31, https://doi.org/10.1175/JCLI-D-17-0047.1, 2018.

Zängl, G., Reinert, D., Rípodas, P., and Baldauf, M.: The ICON (ICOsahedral Non-hydrostatic) modelling framework of DWD and MPI-M: Description of the non-hydrostatic dynamical core, Q.J.R. Meteorol. Soc., 141, https://doi.org/10.1002/qj.2378, 2015.